Author for correspondence:
Muhammad Noman
e-mail: muhammad.noman@uetpeshawar.edu.pk

Boosting efficiency of eco-friendly perovskite solar cell through optimization of novel charge transport layers

Muhammad Ismail[1], Muhammad Noman[1], Shayan Tariq Jan[1,3] and Muhammad Imran[2]

[1]U.S.-Pakistan Center for Advanced Studies in Energy, University of Engineering and Technology, Peshawar, Pakistan
[2]National University of Sciences and Technology (NUST) Rawalpindi, Military College of Signals, Pakistan
[3]Department of Energy Engineering Technology, University of Technology, Nowshera, Pakistan

MN, 0000-0001-8718-6386; STJ, 0000-0002-3914-236X

Formamidinium tin triiodide ($FASnI_3$) is a suitable candidate for the absorber layer in perovskite solar cells (PSC) because of its non-toxicity, narrow band gap, thermal stability and high carrier mobility. This study focuses on the analysis and improvement in the performance of $FASnI_3$-based PSCs using various inorganic charge transport materials. The copper-based materials such as Cu_2O, $CuAlO_2$, CuSCN and $CuSbS_2$ are introduced as hole transport layers due to their earth abundance, ease of manufacturing, high charge mobilities and chemical stability. Similarly, fullerene derivates (PCBM and C_{60}) are deployed as electron transport layers due to their mechanical strength, thermal conductivity and stability. The effect of these materials on optical absorption, quantum efficiency, energy band alignment, band offsets, electric field and recombination are studied in detail. The reasons for the low performance of the cell are identified and improved through design optimization. The PSC performance is analysed in both inverted and conventional architecture. Among all the structures, the best result is achieved through $ITO/CuSCN/FASnI_3/C_{60}/Al$ with an efficiency of 27.26%, V_{oc} of 1.08 V, J_{sc} of 29.5 mAcm^{-2} and FF of 85.6%.

1. Introduction

Over the last decade, perovskite solar cells (PSC) have shown exponential progress in terms of efficiency but structural stability and degradation still remain an obstacle [1]. Perovskites are direct band gap materials with the ABX_3 crystal structure as
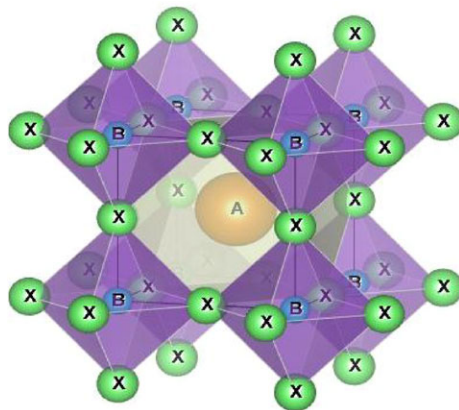
Figure 1. Perovskite ABX$_3$ crystal structure.

shown in figure 1, where 'A' is a monovalent organic cation (Formamidinium, Methylammonium, Cesium, etc.), 'B' is a divalent metal cation (Sn^{+2}, Pb^{+2}) and 'X' is the halogen anion [2,3]. Perovskites are known for their impressive light harvesting properties because of their high absorption coefficient, large diffusion lengths (0.1–1 µm), tunable band gaps and high carrier mobility (1–10 cm^2 V^{-1} s^{-1}) [4].

Lead-based PSC have achieved a breakthrough efficiency of 25.7% but the toxic nature of lead limits its large-scale commercialization [5,6]. To address that problem the toxic lead can be replaced with alternative materials such as Sn, Ge, Bi, Sb and Cu [7]. Sn is considered an adequate replacement for the lead as it is non-toxic, lies in the same group as Pb, and shows higher mobilities (10^2–10^3 cm^2 V^{-1} s^{-1}) than Pb (10–10^2 cm^2 V^{-1} s^{-1}) based perovskites [8].

MASnI$_3$ and FASnI$_3$ are among the high-performing Sn-based perovskites. MASnI$_3$ has a narrower bandgap (1.25 eV) when compared with FASnI$_3$ (1.41 eV), however, it shows less thermal stability [9]. In Sn-based PSC when FA (HC(NH$_2$)$_2^+$) cation is used instead of MA (CH$_3$NH$_3^+$) the temperature stability increases which implies the strong hydrogen bonding between organic HC(NH$_2$)$_2$ and the inorganic matrix [10,11]. FASnI$_3$ shows a higher tolerance factor (because of the large ionic radius of FA cation), higher carrier mobility and low auger recombination when compared with MASnI$_3$ [12,13]. Recent developments in two-dimensional Ruddlesden popper PSC shows that incorporating β-flouroethamamine cations instead of phenyl ethyl ammonium in FA-based PSCs can improve their performance and efficiency up to 16.77% [14]. The Sn-based solar cells show instability when exposed to air which is attributed to the oxidation of Sn^{+2} to Sn^{+4}. Sn^{+4} is not toxic but it behaves like a P-type impurity which consequently decreases PCE (Power Conversion Efficiency) [15]. In FASnI$_3$-based PSC, the extent to which Sn^{+2} converts to Sn^{+4} is less compared with MASnI$_3$-based solar cells. SnX$_2$-based materials are used to tackle this problem [16]. The research also shows that the stability issue regarding the ambient condition can be resolved by incorporating isovalent cations into Perovksite lattice [17]. Until now the highest efficiency reported for FASnI$_3$-based solar cells is 14.6% with PEDOT: PSS used as an HTL [18,19]. Also, impressive efficiency of 13.82% is reported for FASnI$_3$-based PSC with vertical Sn^{+2} gradient using PEDOT: PSS (HTL) and C$_{60}$(ETL) [20].

The performance of the PSC is greatly influenced by the charge transport layers (CTL) in the structure. ETL (Electron Transport Layer) enhances the extraction of photogenerated electrons in the absorber while HTL (Hole Transport Layer) is responsible for the extraction of holes.

Spiro-OMeTAD and PEDOT: PSS as HTLs show high performance with FASnI$_3$ but because of their organic nature they suffer from thermal stability and limited intrinsic hole transport. Both materials have a high cost, complex purification and multistep processing [21,22]. Different inorganic Cu-based materials (CuI, Cu$_2$O, CuAlO$_2$, CuSCN, etc.) are considered promising contenders for HTL because of their desirable characteristics like ease of manufacturing, low production cost, high charge mobility and chemical stability [23]. Similarly, Fullerene (Carbon Allotrope) derivatives such as C$_{60}$ and Phenyl-C61-butyric acid methyl ester (PCBM) are widely used as ETL because of their thermal stability, and electron extraction properties [24,25]. For carbon-based materials like C$_{60}$ and PCBM inverted p-i-n structure is preferred because of the smaller band gap of ETL and their low hysteresis behaviour in an inverted structure [26,27].

In this research, eight unique FASnI$_3$-based solar cells are numerically modelled by using carbon-based ETLs (PCBM and C$_{60}$) and Cu-based HTLs such as Cu$_2$O (cuprous-Oxide), CuAlO$_2$ (Copper

Aluminum Oxide), CuSCN (Copper thiocyanate) and CuSbS$_2$ (Copper Antimony Sulfide). A detailed study is carried out by analysing the effect of thickness, doping concentration, defect density, temperature, back contact electrodes, ARC coating and interface defects on the performance of solar cells. The optimized design parameters for each structure are identified and presented in this study. Moreover, the behaviour of different HTLs is closely analysed by comparing QE, Band Gap and Recombination graphs.

2. Methodology

2.1. Simulation tool

Extensive numerical modelling of the PSC structures is carried out through the simulation tool of SCAPS-1D. It has been developed by the Department of Electronics and Information systems (ELIS), University of Gent, Belgium. It is widely used for the simulation of different types of solar cells including perovskite, CdTe-based and silicon-based solar cells. The software is designed to model a maximum of seven layers for a single-cell structure. It assists in the modification of different solar cell parameters like band gap, defect density, doping, thickness, etc., to achieve better results. The numerical simulation in SCAPS is carried out by solving basic physical differential equations in a steady state such as the Poisson equation (equation (2.1)) and continuity equations (equations (2.2) and (2.3))

$$\frac{\partial^2 \varphi}{\partial x^2} = \frac{q}{\varepsilon}[n - p + N_A - N_D + n_t - p_t], \tag{2.1}$$

$$\frac{i}{J}\frac{\partial J_p}{\partial x} + R_p(x) + G_p(x) = 0, \tag{2.2}$$

$$\frac{i}{J}\frac{\partial J_p}{\partial x} + R_p(x) + G_p(x) = 0, \tag{2.3}$$

$$Jn = qn\,(x)\mu_n E\,(x) + qD_n\,\frac{dn}{dx}, \tag{2.4}$$

$$Jp = qp\,(x)\mu_p E\,(x) + qD_p\,\frac{dp}{dx}, \tag{2.5}$$

$$L_n = \sqrt{D_n . \tau_n}, \tag{2.6}$$

$$L_p = \sqrt{D_p . \tau_p}, \tag{2.7}$$

$$\tau_n = \frac{1}{\sigma \times Nt \times v_{th}} \tag{2.8}$$

$$\text{and} \quad \tau_p = \frac{1}{\sigma \times Nt \times v_{th}}. \tag{2.9}$$

The symbols used in equations (2.1)–(2.8) are mentioned in table 1 along with units and descriptions.

2.2. Device structure

In this study, the inverted p-i-n structures of PSC are modelled as shown in figure 2. It consists of five main layers which are Anode/HTL/absorber/ETL/cathode. Transparent Conduction Oxide (TCO) is the top transparent layer which acts as an anode while the metal electrode is the back layer acting as a cathode. FASnI$_3$ is an absorber layer and is sandwiched between p-doped HTL and n-doped ETL. The function of ETL and HTL is to enhance the charge extraction efficiency and facilitate charge transport (electrons and holes, respectively). In inverted p-i-n structures, ITO is preferred as TCO because of its lower electrical resistivity and higher transparency to the visible spectrum [28]. When light is absorbed by the perovskite layer photogenerated charge carriers are produced in an absorber. Electrons are transferred from the conduction band of the absorber to the conduction band of ETL; similarly, the holes are transferred from the valence band of the absorber to the valance band of the HTL. Metal-electrode (cathode) collects electrons from ETL while TCO (anode) collects holes from HTL. The eight novel structures are modelled in this study and presented in table 2.
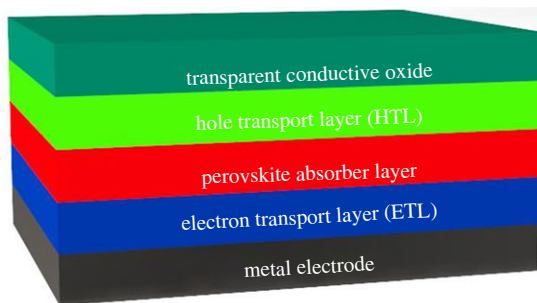
Figure 2. The basic inverted p-i-n solar cell device structure.

Table 1. Description of the physical quantities used in the SCAPs simulator.

symbol	unit	description
φ	V	electro static potential
N_A	cm^{-3}	absorber defect density
N_D	cm^{-3}	donor defect density
q	C	electron charge
ε	F.cm^{-1}	electric permittivity of material
μ	cm^2/Vs	mobility of charge carrier
p	cm^{-3}	hole density
n	cm^{-3}	electron density
G_n, G_p	cm^{3}s^{-1}	generation rate of electron, generation rate of holes
R_n, R_p	cm^{3}s^{-1}	recombination rate of electrons, recombination rate of holes
Dn, Dp	cm^2.s	diffusion coefficient
Jn, Jp	A.cm^{-1}	electron current density, hole current density
L_n, L_p	µ.m	diffusion length of electron, diffusion length of hole
τ_n. τ_p	ns	carrier lifetime electron, carrier lifetime hole
σ	cm^{-2}	electron capture cross-section, hole capture cross-section
Nt	cm^{-3}	total defect density/bulk defect density
v_{th}	V	thermal voltage

Table 2. Group classification of cells.

Group 1 cells	Group 2 cells
ITO/Cu$_2$O/FASnI$_3$/PCBM/Al	ITO/Cu$_2$O/FASnI$_3$/C$_{60}$/Al
ITO/CuAlO$_2$/FASnI$_3$/PCBM/Al	ITO/CuAlO$_2$/FASnI$_3$/C$_{60}$/Al
ITO/CuSCN/FASnI$_3$/PCBM/Al	ITO/CuSCN/FASnI$_3$/C$_{60}$/Al
ITO/CuSbS2/FASnI$_3$/PCBM/Al	ITO/CuSbS2/FASnI$_3$/C$_{60}$/Al

2.3. Device modelling

The design parameters for all the layers (ETL, HTL and FASnI$_3$) have been collected from multiple experimental plus theoretical studies and mentioned in table 3 [10,29–31]. Al with the work function of 4.2 is used as back contact metal while ITO with a work function of 5 is used as front contact in this study. The initial thickness for all CTL is kept at 150 nm. The defect density of ETLs and HTLs is kept at 10^{14} cm^{-3}. For FASnI$_3$ defect density of 2×10^{15} is considered to obtain the carrier lifetime of 2.5 ns which in the literature ranges from 1 to 4 ns [16]. As for the interface defects, single energetic

Table 3. Design parameters for all active layers.

| parameters	FASnI$_3$	PCBM	C$_{60}$	Cu$_2$O	CuAlO$_2$	CuSCN	CuSbS$_2$
thickness (nm)	300	150	150	150	150	150	150
bandgap E_g (eV)	1.41	2	1.7	2.17	3.46	3.4	1.58
electron affinity χ (eV)	3.9	3.9	3.9	3.2	2.5	2.1	4.2
dielectric permittivity	8.2	4	4.2	7.1	60	10	14.6
CB effective density of states (cm^{-3})	10^{18}	10^{21}	8×10^{19}	2.5×10^{20}	2×10^{20}	2.5×10^{18}	2×10^{18}
VB effective density of state N_v (cm^{-3})	10^{18}	2×10^{20}	8×10^{19}	2.5×10^{20}	1×10^{22}	1.8×10^{19}	1×10^{18}
electron mobility μ_n (cm^2 Vs^{-1})	22	10^{-2}	8×10^{-2}	200	2	2×10^{-4}	49
hole mobility μ_p (cm^2 Vs^{-1})	22	10^{-2}	3.5×10^{-3}	8.6×10^3	8.6	2×10^{-4}	49
donor density N_D (cm^{-3})	0	10^{20}	2.6×10^{17}	0	0	0	0
acceptor density N_A (cm^{-3})	7×10^{16}	0	0	10^{19}	10^{20}	10^{17}	10^{18}
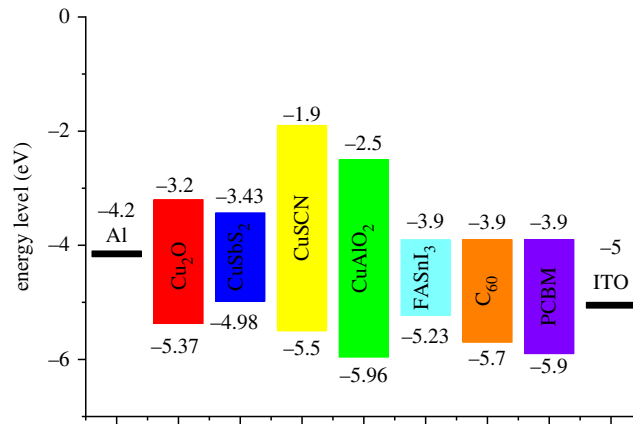
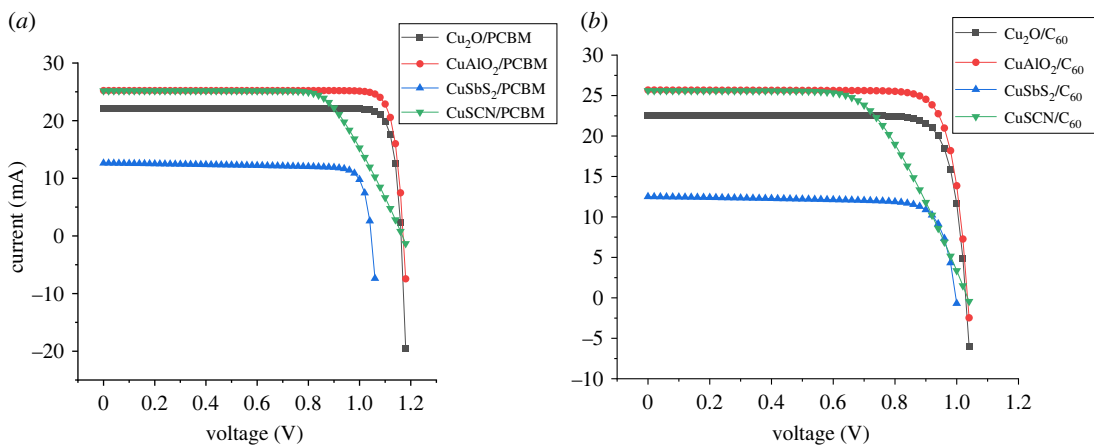**Figure 3.** Energy level diagram for different active layers of PSC.

Figure 4. I–V curves for simulated cells in (*a*) Group 1 and (*b*) Group 2 cells.

Table 4. Absorber defect density and interface defects parameters.

	ETL/absorber	HTL/absorber	FASnI$_3$
defect type	neutral	neutral	neutral
capture cross-section of electrons and holes (cm^{-2})	1×10^{-15}	1×10^{-15}	1×10^{-15}
energetic distribution	single	single	gaussian
energy level w.r.t to E_v	0.6	0.6	0.6
characteristic energy (eV)	—	—	0.1
total density (cm^{-3})	1×10^{10}	1×10^{10}	2×10^{15}

distribution is incorporated alongside other parameters mentioned in table 4. All the simulations are carried out under AM 1.5 radiation with solar irradiance of 1000 W m^{-2} and at room temperature (300 K).

The energy level diagram for all the layers is shown in figure 3. The IV cure obtained for the different structures is shown in figure 4 while the characteristics are presented in table 5.

2.4. Device behaviour

2.4.1. IV characteristics

The squareness of the I–V curve or in other words FF determines the parasitic losses (series and shunt losses) present in solar cells. The higher the FF values the lower the parasitic losses. FF is strongly

Table 5. Initial Performance Parameters for non-optimized cells.

cells	V_{oc}	J_{sc}	FF	PCE %
ITO/Cu$_2$O/FASnI$_3$/PCBM/Al	1.127	22.129	86.634	21.608
ITO/CuAlO$_2$/FASnI$_3$/PCBM/Al	1.133	25.200	86.197	24.611
ITO/CuSbS$_2$/FASnI$_3$/PCBM/Al	1.043	12.618	82.322	10.839
ITO/CuSCN/FASnI$_3$/PCBM/Al	1.167	25.178	69.966	20.569
ITO/Cu$_2$O/FASnI$_3$/C$_{60}$/Al	1.029	22.524	83.410	19.330
ITO/CuAlO$_2$/FASnI$_3$/C$_{60}$/Al	1.034	25.633	82.892	21.979
ITO/CuSbS$_2$/FASnI$_3$/C$_{60}$/Al	0.996	12.491	79.475	9.897
ITO/CuSCN/FASnI$_3$/C$_{60}$/Al	1.035	25.610	62.878	16.675

related to series resistance [32]. An increase in series resistance results in a decrease in FF.

$$\text{FF} = \text{FF}_o \left(1 - R_s \frac{J_{sc}}{V_{oc}} \right), \tag{2.10}$$

where R_s is series resistance, FF_o is the value of *FF* at $R_s = 0 \, \Omega \, \text{cm}^2$. R_s includes TCO series resistance, resistance in charge transport at the interface, and the bulk of the solar cell.

Among the proposed cells for given ETL (C$_{60}$ or PCBM), Cu$_2$O-based cells show better IV behaviour in figure 4 followed by CuAlO$_2$, while CuSCN shows clear signs of series resistance.

2.4.2. Optical absorption

In p-i-n structures, HTL acts as a front layer after TCO. For maximum photons to reach the perovskite layer, it is required that HTL possesses a minimum optical absorption with maximum transmittance. Materials with low absorption coefficients possess high transmittance values. The absorbance and transmittance of a material can be related by the following equation:

$$\alpha = \frac{\ln(1/T)}{d}. \tag{2.11}$$

Where α is an absorption coefficient, T represents transmittivity and d is the film thickness.

The absorption coefficient depends upon the optical band gap of the material. Materials with higher optical band gap values have low optical absorption. The absorption coefficient of material as a function of wavelength can be related to the optical band gap of material by the following equation:

$$\alpha(\lambda) = \left(A + \frac{B}{h\nu} \right) \sqrt{(h\nu - E_g)}, \tag{2.12}$$

where $h\nu$ represents the photon energy and E_g represents the band gap of a material.

Materials with large band gaps have transmissivity for low-energy photons, allowing them to pass through without being absorbed. Absorption in films in transparent regions may occur due to scattering of light, defect absorption, and multi-phonon absorption or Urbach tail [33–35]. Figure 5 shows that CuSCN and CuAlO$_2$ have high transmittance to the photons with a wavelength greater than 350 nm which include the visible spectrum (400–700 nm). Among the above-mentioned HTLs CuAlO$_2$ ($E_g = 3.46$) has maximum transmittance followed by CuSCN ($E_g = 3.4$), Cu$_2$O ($E_g = 2.17$) and CuSbS$_2$ ($E_g = 1.58$), respectively. The transmittance of a material depends on a variety of factors including preparation methods, deposition methods and also thickness of the layer [33,36].

2.4.3. Quantum efficiency

QE or IPCE (incident photon to current efficiency) is the measure of electrons collected by a solar cell in response to the incident photons at a certain wavelength. QE at different wavelengths represents the spectral response of different solar cells to the incident light. It can be calculated from the
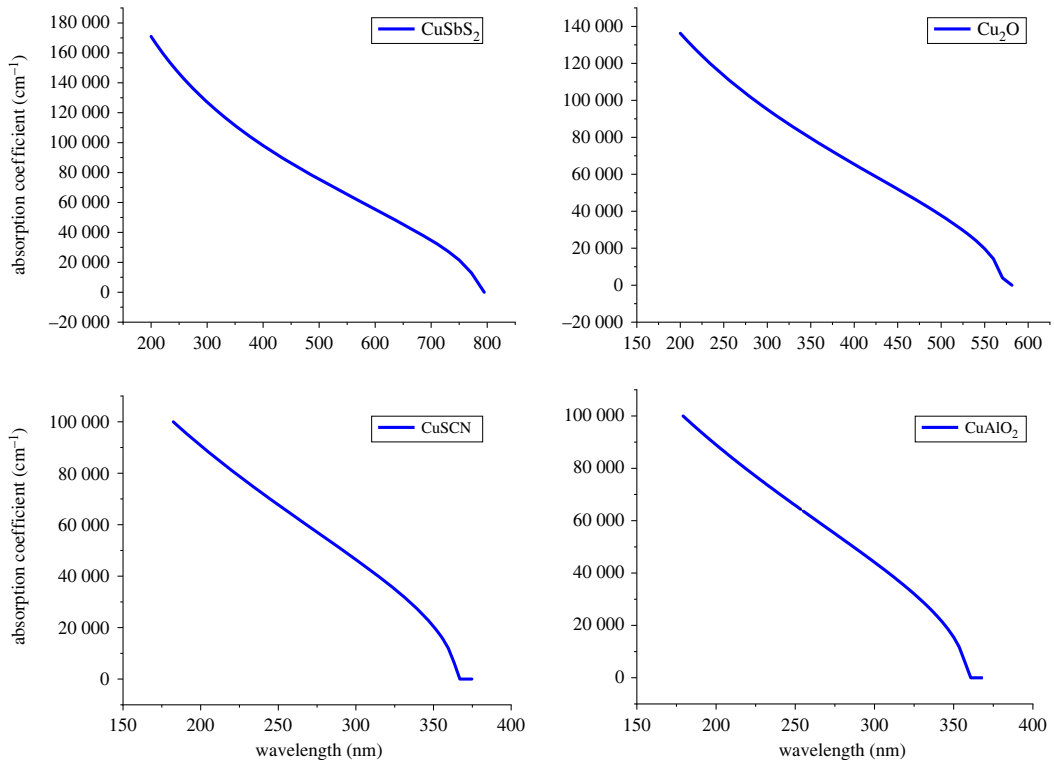
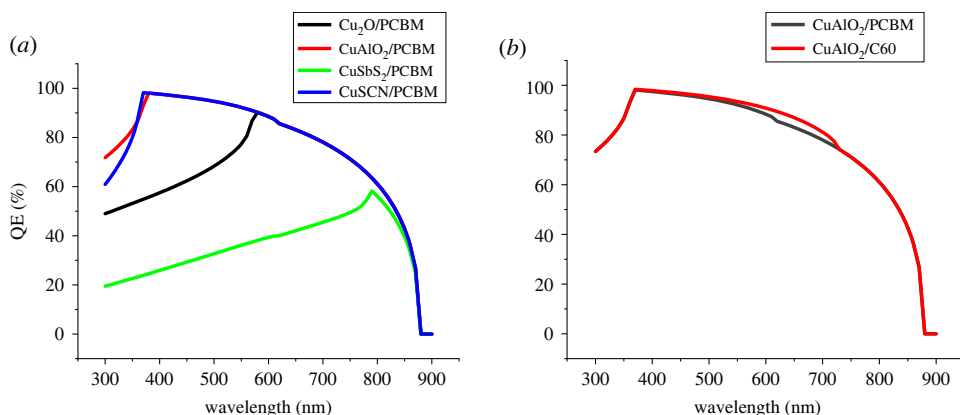**Figure 5.** The optical absorption of the HTLs.

Figure 6. Effect of different CTL on QE of the cell (*a*) HTL and (*b*) ETL.

following equation:

$$QE = \frac{\text{no. of reacted electrons}}{\text{no. of incident photons}}. \tag{2.13}$$

Figure 6*a,b* shows different QE peaks for the solar cells on the basis of HTLs and ETL listed in table 4. The shift in peaks can be closely related to the absorption curves of HTLs in figure 5. The QE of the charge transport layer in figure 6 rises for the wavelengths where the absorption coefficient of the material is minimum. The smaller the absorption coefficient the higher the transparency and thus more photons reach the absorber layer through HTLs which increases QE.

2.4.4. Energy band alignment

Band gap alignment plays an important role in determining the performance of solar cells. It determines how well an absorber performs with a set of CTL. As can be seen in figure 3 each material has different
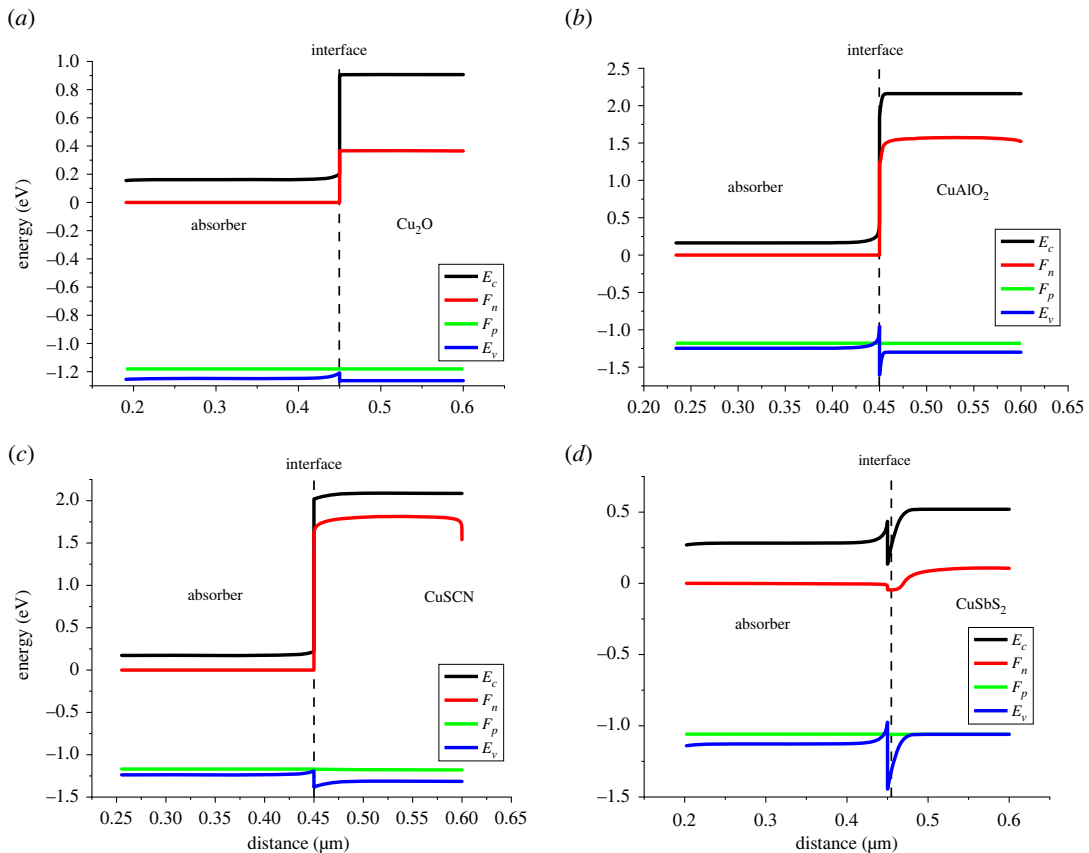
Figure 7. Band alignment at (*a*) absorber/Cu$_2$O, (*b*) absorber/CuAlO$_2$, (*c*) absorber/CuSCN interfaces and (*d*) absorber/CuSbS$_2$.

energy levels, therefore forming different energy band alignments and band offsets. Figure 7 shows the band gap alignment at the absorber/HTL interface. The function of HTL is not only to transport holes from the absorber but also to block electrons from the absorber [37]. For the efficient transport of holes, minimum valence band offset (VBO) is required at the absorber/HTL interface, while for blocking electrons from the absorber, maximum conduction band offset (CBO) is required.

The key energy levels (figure 7) in a photovoltaic cell are the conduction band (E_c), the Fermi level for the n-type material (F_n), the Fermi level for the p-type material (F_p) and the valence band (E_v).

— The conduction band (E_c) is highest energy level in the solid where electrons can freely move and is made of LUMO (lowest molecular orbital) of semiconductor.
— The Fermi level for the n-type material (F_n) is the energy level at which the probability of occupation of an electron is 0.5. The significance of this level is that it separates the energy levels where electrons are likely to be found from the energy levels where they are unlikely to be found. In an n-type semiconductor or ETLs, the Fermi level is near the conduction band due to the excess of electrons.
— Similarly at Fermi level for p-type semiconductors (F_p) the probability of finding holes occupation is 0.5 at absolute temperature. In a p-type semiconductor or HTLs, the Fermi level is close to the valence band because of excess holes.
— The valence band (E_v) is the lowest energy level in the solid where electrons are tightly bound to the atoms and cannot move freely. In a solar cell, the valence band is typically made up of the highest occupied molecular orbital (HOMO) of the semiconductor material.

These energy bands are arranged in such a way as to facilitate the charge transport in solar cells. When light falls on perovskite (absorber layer) e-h pairs are produced as the electrons are excited from valence to conduction band. The electrons in the conduction band of absorber layer move conduction n-type material (ETL); similarly the holes in the absorber layer move to the valence band of absorber to the valence band of p-type material. These charge carriers are then collected by electrodes.

The Fermi levels of the n-type and p-type layers provide a built-in potential barrier at heterojunction. This potential barrier ensures that the electrons and holes are separated and prevented from recombining.

Table 6. VBO and CBO at the absorber/HTL interface.

absorber/HTL interface	CBO	VBO
FASnI$_3$/Cu$_2$O	+0.7	+0.06
FASnI$_3$/CuAlO$_2$	+1.4	+0.65
FASnI$_3$/CuSCN	+1.8	+0.19
FASnI$_3$/CuSbS$_2$	−0.3	+0.47

The built-in potential barrier also creates a driving force for the electrons and holes to move towards the electrodes and contribute to the overall current generated by the solar cell.

Two types of discontinuities occur in response to band offset at the interface: positive and negative. If the absorber's conduction band is higher than the conduction band of the CTL, it forms a negative cliff (–CBO) at the heterojunction. While, if the absorber's conduction band is beneath the conduction band of the CTL, it forms a positive spike (+CBO) at the heterojunction [38–40]. Similarly, cliff and spike are also formed by the valance band at the heterojunction. VBO and CBO at the absorber/HTL interface can be calculated through the following equations:

$$VBO = \chi_{HTL} - \chi_{Per} + E_{g_{HTL}} - E_{g_{Perov}} \tag{2.14}$$

and

$$CBO = \chi_{Per} - \chi_{HTL}. \tag{2.15}$$

For all the HTLs spike discontinuity was observed at the valence band shown in table 6 and figure 7. Cu$_2$O forms the best band alignment with a smaller VBO (spike) of 0.06 eV thus facilitating the hole transport and higher CBO value of 0.7 eV, blocking the leaked electrons from the absorber. This ensures the smooth flow of holes and the blockage of electrons. The small spike, i.e. with VBO < 0.4 eV, facilitates the flow of holes at the interface because of high built-in potential (V_{bi}) values, thus resulting in a drop in recombination [38,41]. The large spike (VBO > 0.4 eV) hinders the flow of the holes because it forms low V_{bi} values at the interface and resulting in low V_{oc} values [42]. V_{bi} can be related to the V_{oc} by the following relation:

$$V_{oc} = V_{bi} - \frac{nKT}{q} \ln \frac{J_o}{J_L}. \tag{2.16}$$

As can be seen in table 4 large spikes (VBO > 0.4 eV) are observed at the absorber/CuSbS$_2$ and absorber/CuAlO$_2$ interface. The worst alignment can be observed at the absorber/CuSbS$_2$ interface because of large spike of +0.47 eV, thus hindering the flow of holes and smaller CBO of (−0.3 eV) which might result in the leakage of electrons towards the HTL side.

The main purpose of ETL is to facilitate the smooth transfer of electrons as well as the blockage of holes from the absorber layer which can be controlled by band alignment. Figure 8 shows band gap alignment at ETL and absorber interface. For smooth electron transport to take place minimum CBO at the ETL/absorber interface is required and to block leaked holes from the absorber maximum VBO is preferred at the interface. The VBO and CBO at the ETL/absorber interface are mentioned in table 7.

2.4.5. Electric potential at heterojunction

Electron and hole transport layers play an important role in facilitating the transport of charge carriers produced in the absorber layer. The charge carriers produced at the absorber layer are transferred to the ETL or HTL as a result of a strong electric potential/electric field at the absorber/CTL interface due to band alignment. Figures 9 and 10 show the electric potential values at the absorber/HTL and ETL/absorber interface, respectively. The high values of the electric field increase the conductivity of charge carriers and reduce recombination leading to a high value of V_{oc}. The electric field at the interface is caused by quasi-fermi level splitting at the absorber/CTL interface [43]. When the difference between fermi levels increases the electric field at the interface increases leading to high
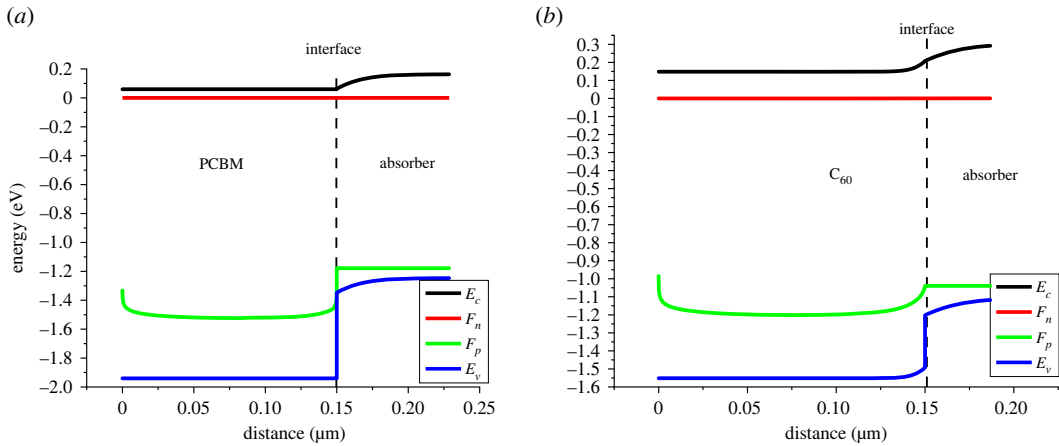
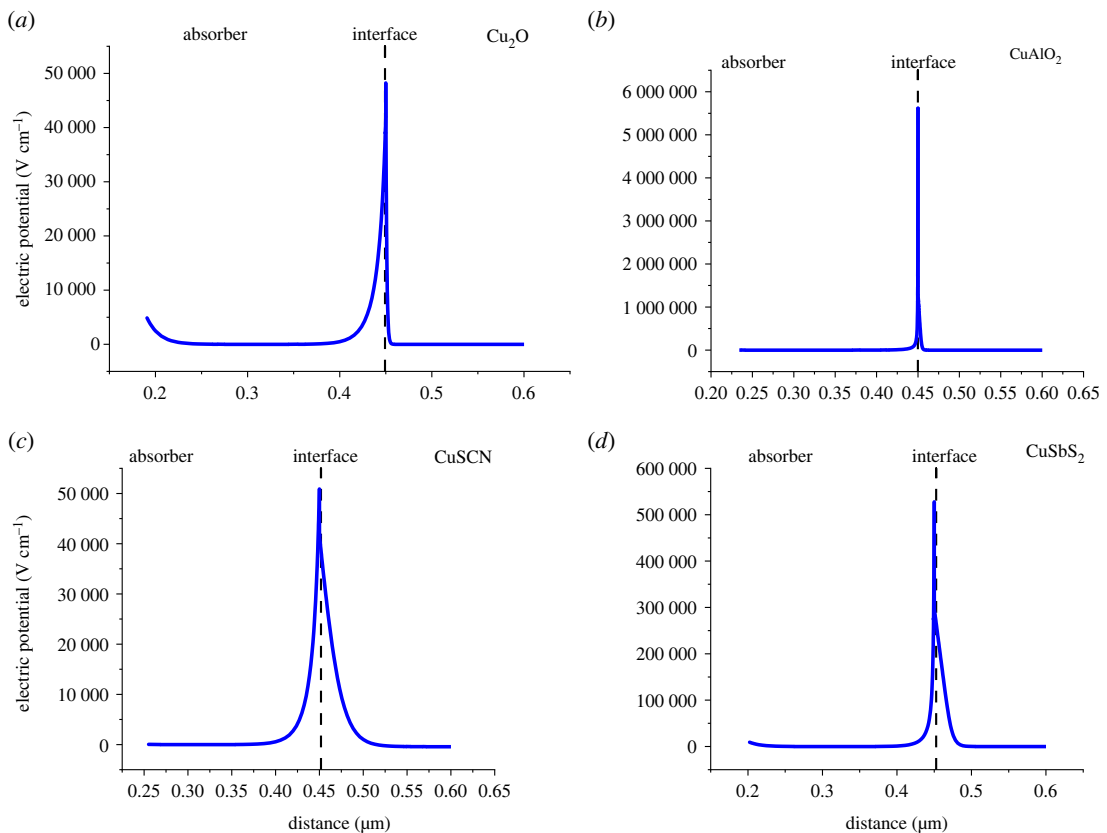**Figure 8.** Band alignment at (*a*) PCBM/absorber interface and (*b*) C_{60}/absorber interface.

Figure 9. Electric potential at (*a*) absorber/Cu_2O, (*b*) absorber/$CuAlO_2$, (*c*) absorber/CuSCN and (*d*) absorber/$CuSbS_2$ interfaces.

Table 7. VBO and CBO at ETL/absorber interface.

ETL/absorber interface	CBO	VBO
PCBM/FASnI$_3$	0	+0.59
C$_{60}$/FASnI$_3$	0	+0.29

V_{oc} [44]. Fermi level difference/splitting (ΔE_F) is related to V_{oc} through the following equation:

$$\Delta E_F = q V_{oc}. \tag{2.17}$$

As the results show in figure 9*b*, the absorber/$CuAlO_2$ shows the highest electric potential values at the interface.
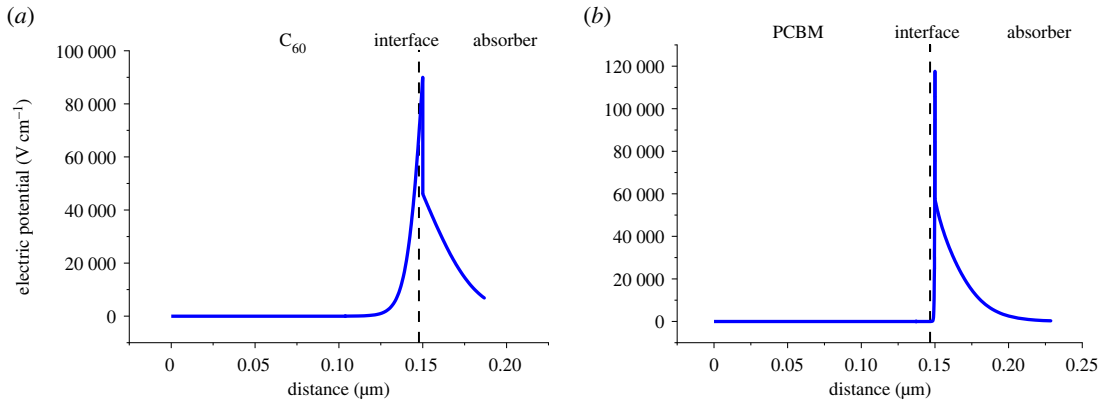
Figure 10. Electric potential at (*a*) C_{60}/absorber interface and (*b*) PCBM/absorber interface.
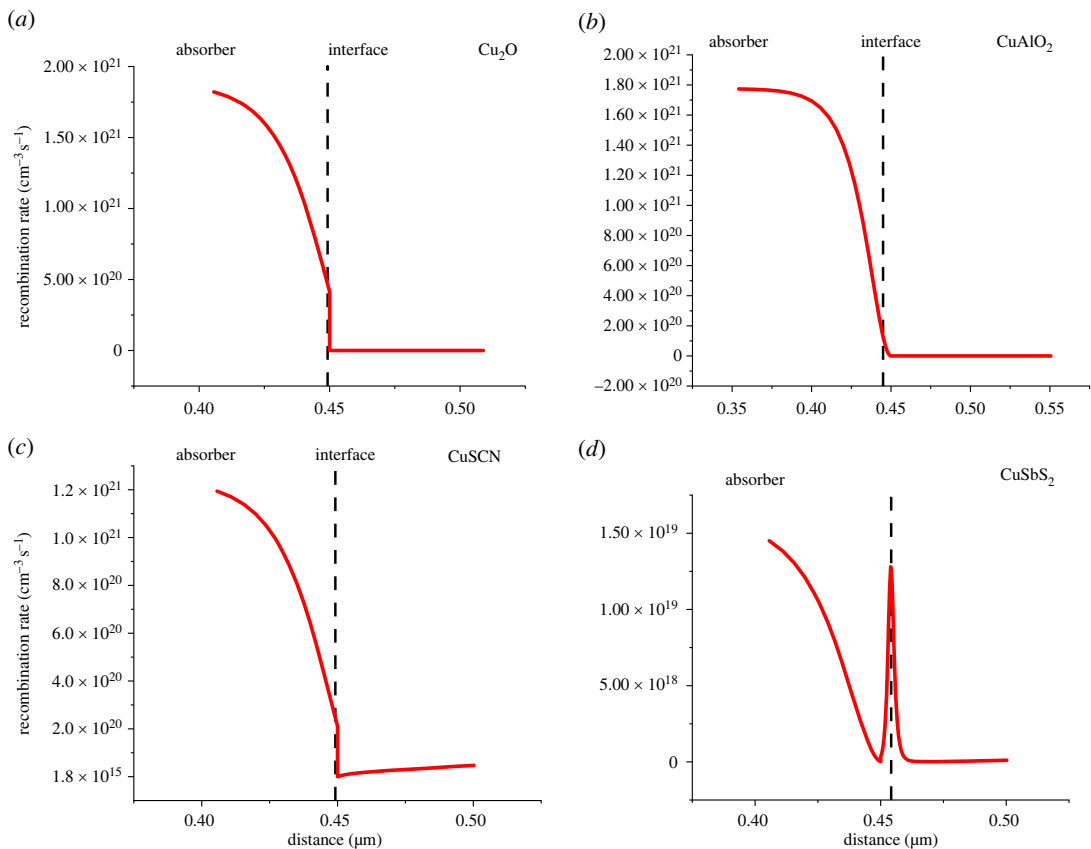

Figure 11. Recombination at (*a*) absorber/Cu_2O, (*b*) absorber/$CuAlO_2$, (*c*) absorber/CuSCN interfaces and (*d*) absorber/$CuSbS_2$.

2.4.6. Recombination at heterojunction

Recombination at the interfaces is highly dependent upon the VBO and CBO values. As values for VBO mentioned in table 6 large spikes occur at the absorber/$CuSbS_2$ and absorber/$CuAlO_2$ interface. Because of the large spike the charges accumulate at the interface resulting in recombination rise as can be seen in figure 11*d*. However, the recombination decreases at absorber/$CuAlO_2$ as shown in figure 11*b*, despite having a larger spike, because $CuAlO_2$ is highly doped ($N_A = 10^{20}$ cm^{-3}). As a result of this Fermi level splitting at the interface is high which develops a strong electric field at the interface as shown in figure 9*b*, thus improving charge transport and reducing the recombination rate [44].

Figure 12 shows a rise in recombination rate at the C_{60}/absorber interface while at the PCBM/ absorber interface it is decreasing. The increase in recombination at the C_{60}/absorber interface is because the VBO (0.29 eV) is less than 0.4 eV, because of which the holes are leaking towards the ETL which is increasing the recombination.
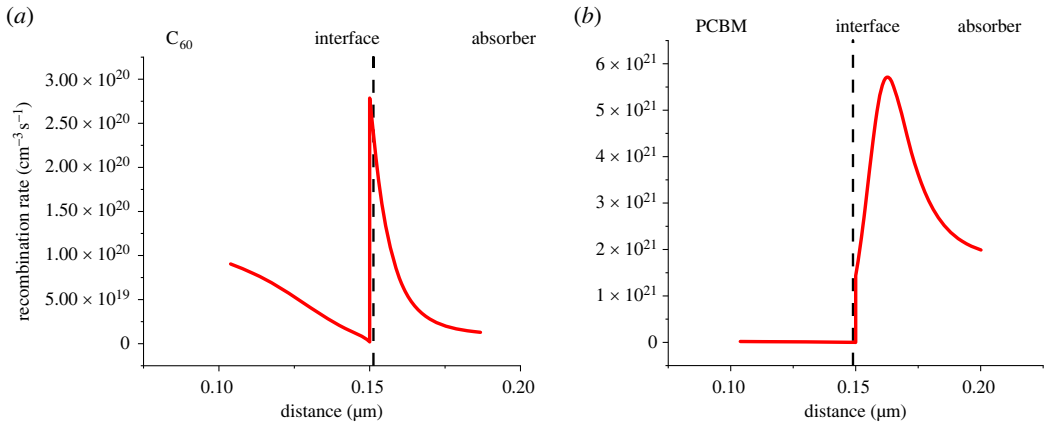
(*a*)

(*b*)

Figure 12. Recombination at (*a*) C_{60}/absorber interface and (*b*) PCBM/absorber interface.

3. Results and discussion

3.1. Absorber and charge transport layers thickness optimization

Absorber layer thickness has a great effect on the performance of solar cells, influencing absorption, generation and charge transport. The effect of absorber thickness is analysed by varying thickness from 50 nm to 1500 nm (50 nm increment) while keeping all the other device parameters shown in table 3 constant. The optimum results were observed at different thickness values mentioned in table 8. With the absorber thickness increase, the increase in V_{oc}, PCE, FF and J_{sc} is observed as shown in figure 13. A thicker absorber layer can absorb a wide range of photons resulting in more charge carrier generation which leads to the increase in J_{sc}. It also causes a decrease in the effective band gap, thus photons of larger wavelengths are also absorbed [45,46]. When the thickness is low, the photons of larger wavelengths and low energy are not absorbed. Therefore, a moderate thickness of the absorber is required. The absorber thickness depends greatly upon the diffusion length and absorption coefficient of the material.

After achieving optimum thickness, further increase leads to saturation and eventually a decrease in PCE and FF. This is due to the absorber thickness exceeding the carrier diffusion length, making the charge carriers unable to reach the CTL resulting in a decrease in performance because of an increase in recombination. The thickness of the absorber can be increased up to the diffusion length of a material [16]. The optimum results were observed at different thickness values mentioned in table 8.

The CTL (ETL and HTL) in solar cells not only serve the purpose of charge transport from the absorber to the respective electrodes but also play the role of separation layer between the absorber and electrode [47].

After the optimization of absorber thickness, ETL thickness was optimized by varying thickness from 50 nm to 350 nm keeping the absorber and HTL thickness constant. Once the optimum thickness for ETL was determined, HTL thickness was optimized keeping both ETL and absorber at optimized thickness values. In p-i-n inverted solar cells, HTL being the front layer has a major effect on performance which decreases with an increase in thickness. The decrease in performance is because of the decrease in transparency with thickness. While ETL thickness has a negligible effect on solar cell performance as shown in figures 14 and 15. So, for all calculations, ETL thickness is kept at 100 nm to achieve the purpose of separating the layer. By increasing the thickness of HTL, the series resistance between the absorber and HTL increases, resulting in a decrease in V_{oc} and leading to a drop in FF, J_{sc} and PCE.

3.2. Optimization of absorber and charge transport layers doping

To investigate the optimization of absorber doping, its acceptor doping density N_A is varied from 10^{12} to 10^{18} cm^{-1} while keeping the thickness of an absorber and CTLs at optimized values. Absorber doping increases the performance of solar cells because it increases the density of majority charge carriers and hence improves conductivity and reducing recombination rate [48,49]. Figure 16 shows that when the
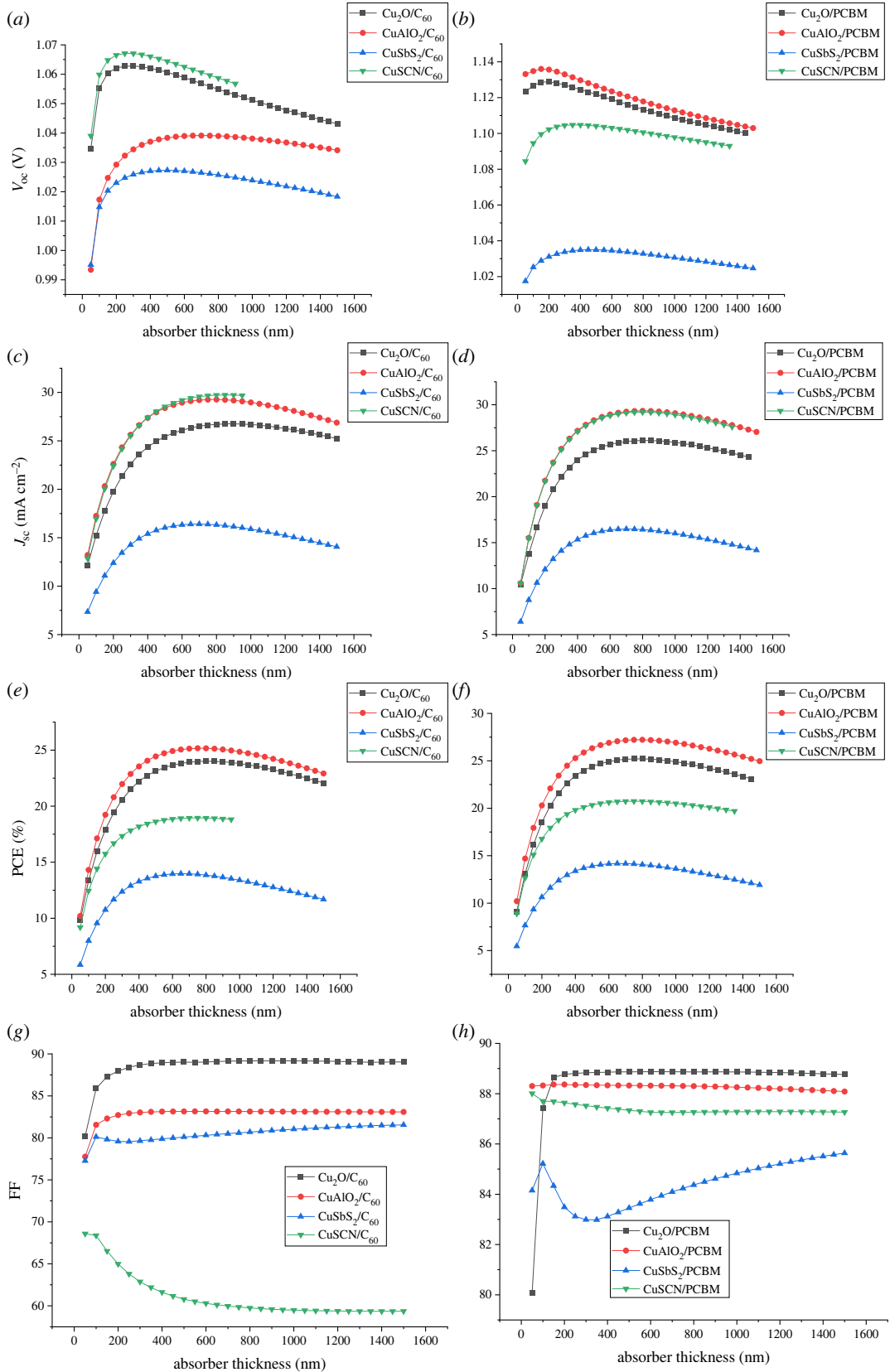
Figure 13. Effect of absorber thickness on (a,b) V_{oc}, (c,d) J_{sc}, (e,f) PCE and (g,h) FF.

doping is increased from 10^{14} cm^{-1} to 10^{16} cm^{-1}, the performance of cells is increasing because of an increase in the electric field across the absorber interface. The electric field facilitates the charge separation which translates to an increase in PCE and V_{oc} [47]. However, as N_A is increased above
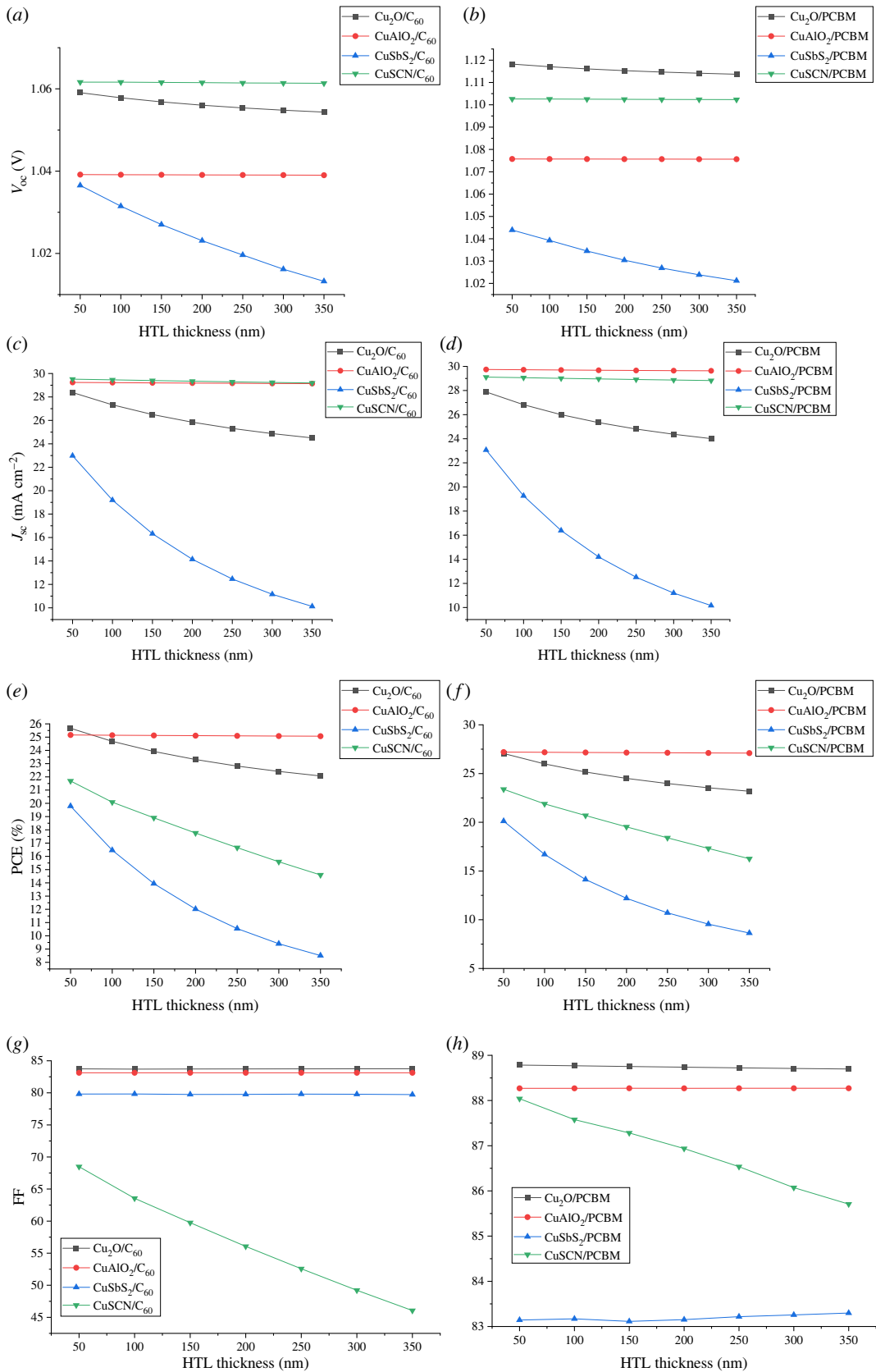
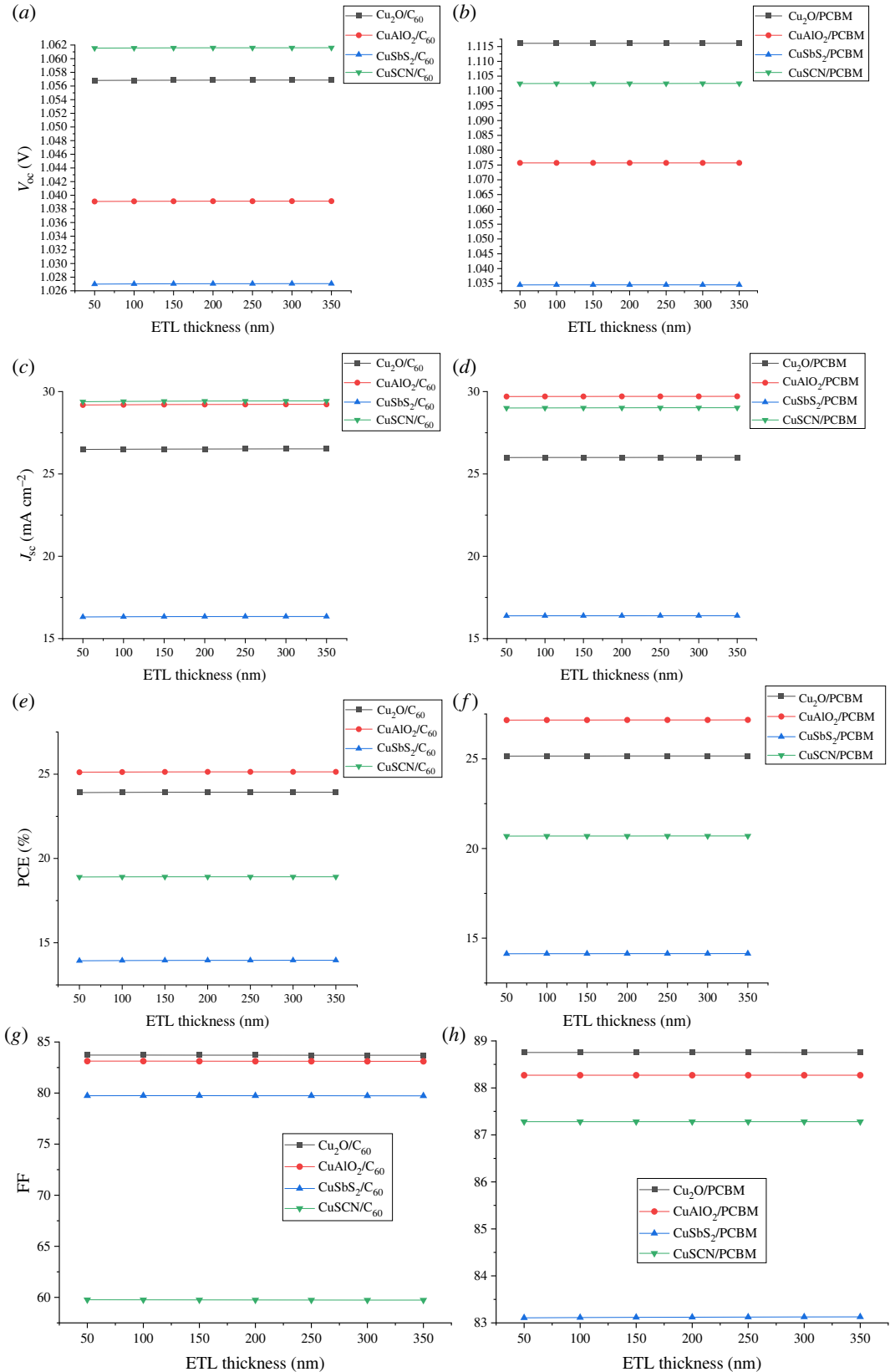**Figure 14.** Effect of HTL thickness on (a,b) V_{oc}, (c,d) J_{sc}, (e,f) PCE and (g,h) FF.

Figure 15. Effect of ETL thickness on (a,b) V_{oc}, (c,d) J_{sc}, (e,f) PCE and (g,h) FF.

10^{16} for some cells, a sudden drop is observed which is implied by the fact that at higher doping values auger recombination dominates. Increasing N_A leads to suppression in charge transportation and a decrease in charge mobilities (μ_n and μ_p) due to an increase in ionized impurity scattering [50]. The sudden increase in V_{oc} PCE and J_{sc} in a majority of cells at very high doping (above 10^{17} cm^{-1})
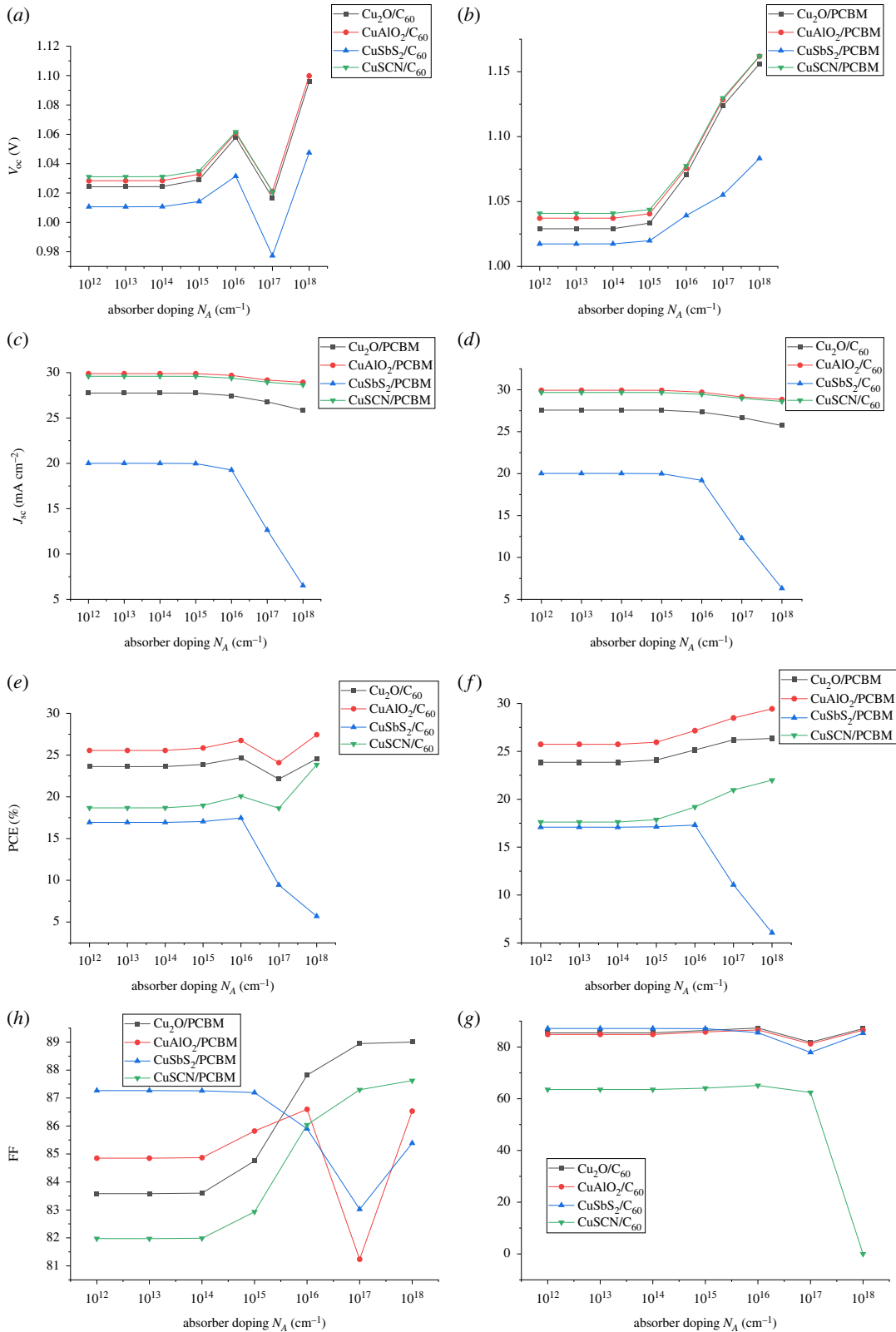
Figure 16. Effect of absorber doping on (a,b) V_{oc}, (c,d) J_{sc}, (e,f) PCE and (g,h) FF.

absorber starts losing its semiconductor behaviour and adopting metallic properties [47]. The optimum doping of absorber of 10^{16} was selected for all the cells.

After the optimization of absorber doping the optimization of ETL and HTL is performed. The doping density of ETL (N_D) and HTL (N_A) is varied from 10^{14} cm^{-1} to 10^{20} cm^{-1}. Doping of CTL improves the conductivity of charge by enhancing the electric field at the absorber and CTL interface.
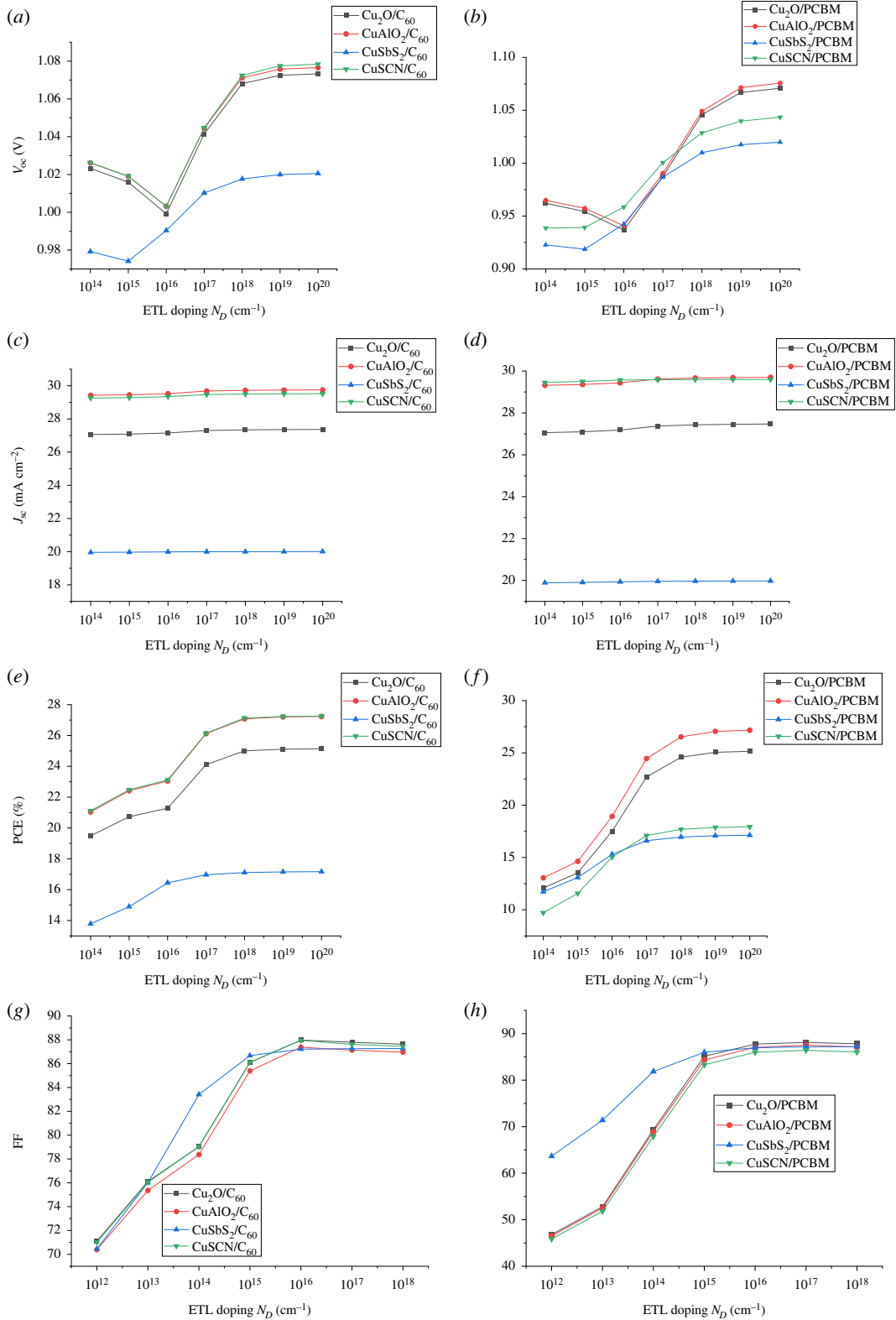
Figure 17. Effect of ETL doping (N_D) on (a,b) V_{oc}, (c,d) J_{sc}, (e,f) PCE and (g,h) FF.

The increase in doping increases the fermi level difference at the absorber/CTL interface developing a strong electric field that facilitates the charge transport to respective electrodes [51]. The electric field at the ETL/absorber interface helps in electron extraction, i.e. facilitating the transfer of electrons (majority charge carriers) and blocking holes (minority charge carriers). Similarly, the electric field at the absorber/HTL interface attracts holes (majority charge carriers) toward HTL while repelling the electrons (minority charge carriers). The increase in FF, PCE, V_{oc} and J_{sc} as a result of the increase in
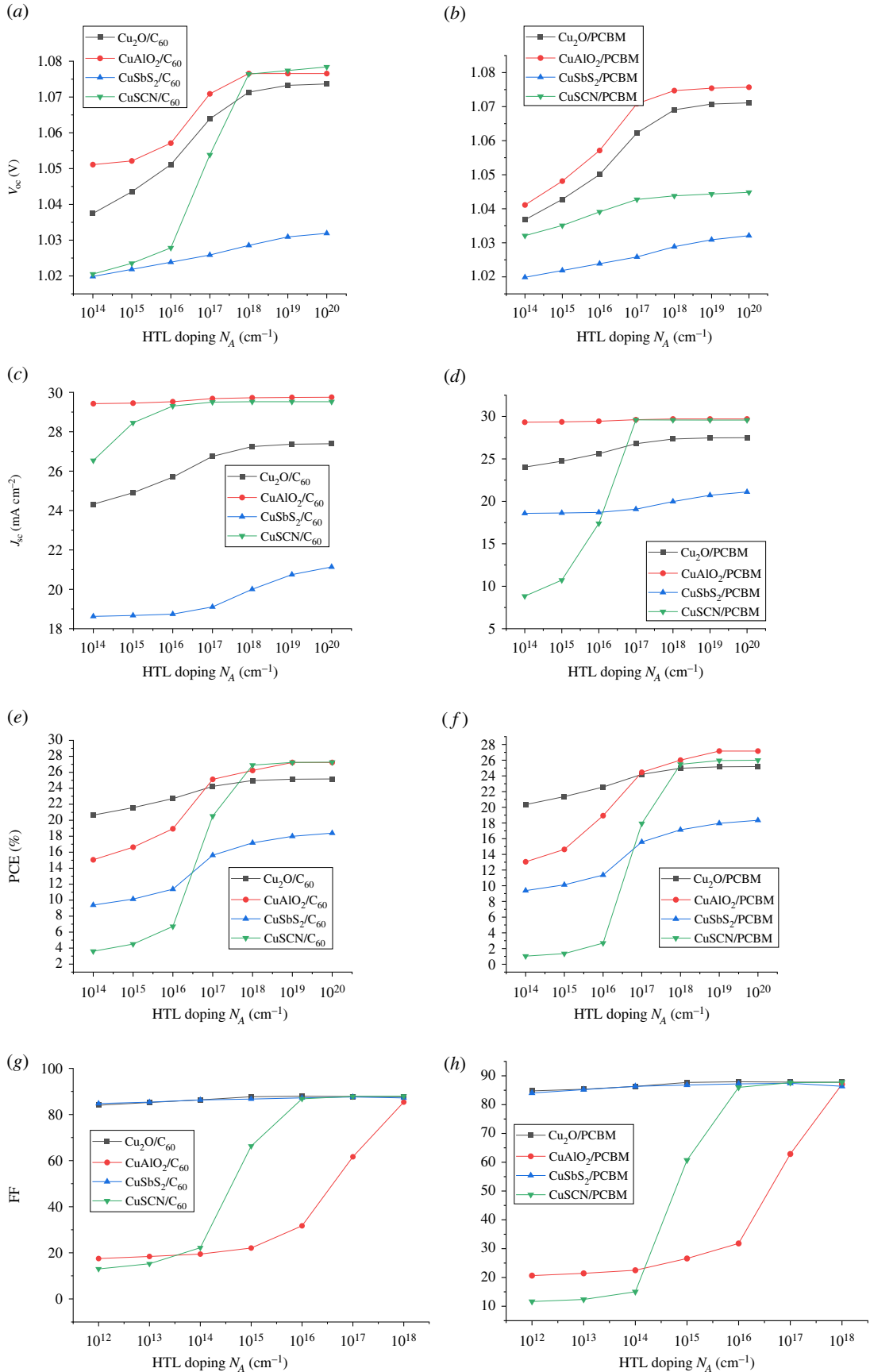
Figure 18. Effect of HTL doping (N_D) on (a,b) V_{oc}, (c,d) J_{sc}, (e,f) PCE and (g,h) FF.

Table 8. Performance parameters of optimized cells.

cells	absorber thickness (nm)	HTL thickness (nm)	V_{oc}	J_{sc}	FF	PCE
ITO/Cu$_2$O/FASnI$_3$/PCBM/Al	750	100	1.071	27.494	85.519	25.185
ITO/CuAlO$_2$/FASnI$_3$/PCBM/Al	700	150	1.076	29.702	85.019	27.164
ITO/CuSbS2/FASnI$_3$/PCBM/Al	600	100	1.034	21.110	84.015	18.340
ITO/CuSCN/FASnI$_3$/PCBM/Al	550	100	1.0438	29.572	84.217	25.996
ITO/Cu$_2$O/FASnI$_3$/C$_{60}$/Al	700	100	1.074	27.389	85.587	25.169
ITO/CuAlO$_2$/FASnI$_3$/C$_{60}$/Al	700	150	1.077	29.753	85.027	27.235
ITO/CuSbS$_2$/FASnI$_3$/C$_{60}$/Al	600	100	1.035	21.135	84.028	18.386
ITO/CuSCN/FASnI$_3$/C$_{60}$/Al	650	100	1.078	29.524	85.621	27.260

ETL and HTL doping can be seen in figures 17 and 18, respectively. The optimized values for CTLs (ETL and HTL) are taken as 10^{20} cm^{-1}.

3.2.1. Optimized solar cell parameters

The optimized results obtained as a consequence of the thickness and doping optimization are mentioned in table 8. As mentioned in the Results, the optimized thickness value for all ETLs is considered 100 nm. The absorber doping for all the cells was selected to be 10^{16} cm^{-1} while the CTLs doping is taken at 10^{20} cm^{-1}.

3.3. Effect of absorber defect density

Defect density is an important parameter for determining the performance of an absorber. The important processes like recombination, generation and absorption that occur in the absorber layer are highly dependent on its defect density and film quality [29,52]. Poor film quality results in an increase in defect density. Defects act as recombination centres and enhance the recombination rate. In PSC, Trap-assisted Shockley–Read–Hall (SRH) recombination (non-radiative recombination) is dominant as compared to other types of recombination [53,54] and is represented by the following equation:

$$R_{SRH} = \frac{np - n_i^2}{\tau(p + n\, 2ni \cosh(E_i - E_t / KT))}.$$ (3.1)

This type of recombination occurs through localized energy states called traps between valance and conduction bands created as a result of doping or defect in the crystal lattice. An increase in defect density (N_t) results in a decrease in a carrier lifetime (τ) of charge carriers which results in a decrease in carrier diffusion length and an increase in non-radiative recombination (R_{SRH}) which results in the degradation of the PCE of the cell [55]. The effect of defect density on an absorber layer is analysed by varying its defect density from 10^{13} to 10^{18} (cm^{-1}), keeping all optimized thickness and doping values constant as shown in figure 19.

3.4. Effect of interface defects

Interface defects arise in PSCs at the interfaces of the absorber and CTL because of the energy level alignment of both layers in addition to trap defect densities. Recombination through traps depends upon a variety of factors including trap density (N_t) energy level of trap state (E_t) and electron and hole cross-section [56]. Two types of defects occur because of the energy level of trap states. Shallow defects occur when E_t lies close to E_V or E_c while defects occur when the defect lies close to mid of E_g [57].

To observe the effect of interface defect density, the energy level of the trap is considered 0.6 eV above E_v. The recombination in an interface is evaluated by the Pauwels–Vanhoutte theory which is an extension of SRH theory. The increase in interface defects increases the number of traps and the resistance at an interface leading to recombination and reduction in the cell's performance. Two interfaces (ETL/ absorber and absorber/HTL) form when the absorber comes into contact with the corresponding CTLs. In order to analyse the effect at interfaces, defect density is increased from 10^{10} to 10^{16} for both ETL/
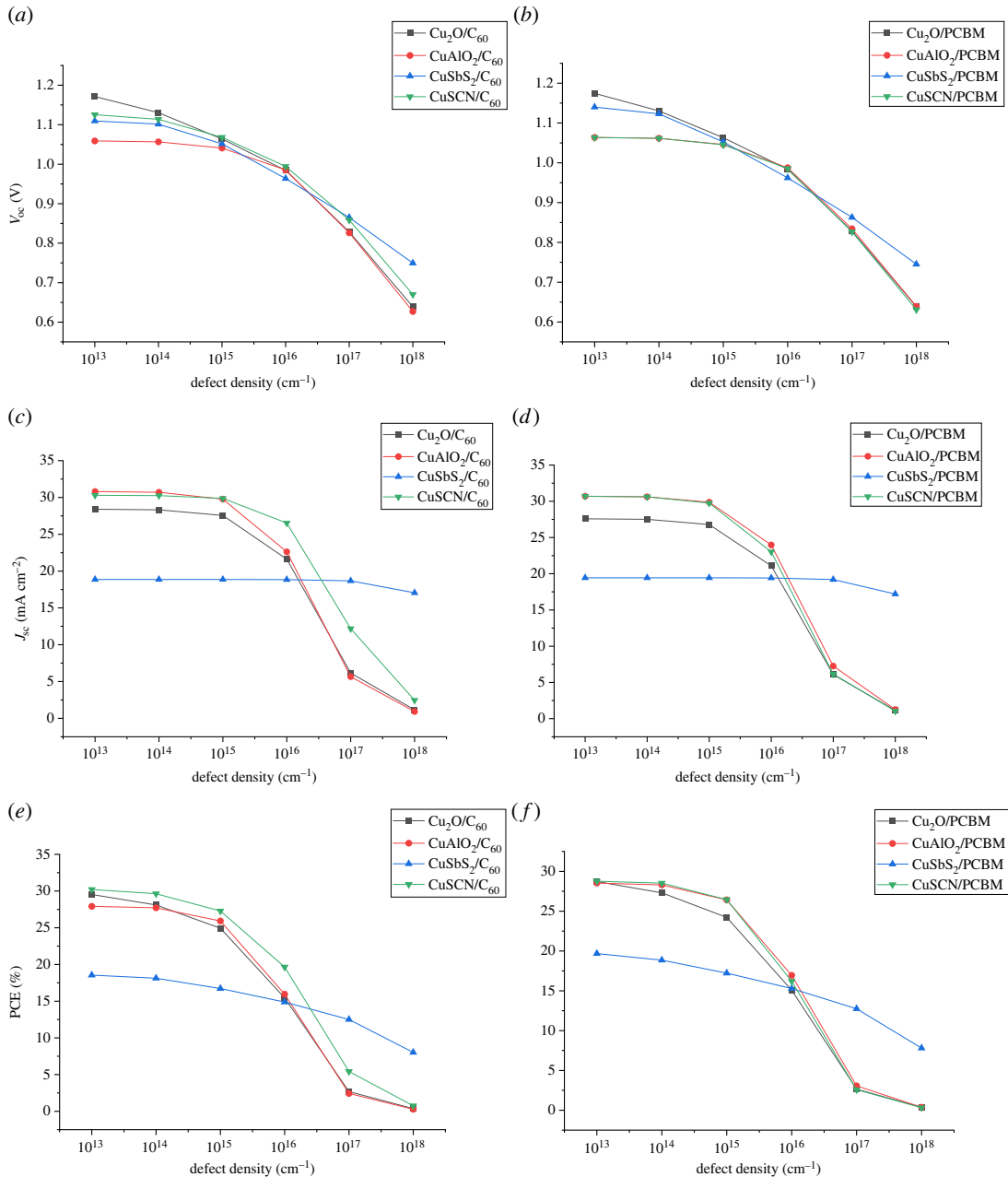
Figure 19. Effect of variation in absorber defect density on (a,b) V_{oc}, (c,d) J_{sc} and (e,f) PCE.

absorber interface and absorber/HTL interface as shown in figures 20 and 21. It has been observed for absorber/ETL that the increase in defect density results in the decrease of V_{oc} leading to a drop in PCE. The reduction in V_{oc} is because charge carriers (holes) recombine through increasing number of traps states as a result of an increase in defect density. The interface defect density can be controlled by reduction in crystallographic and surface defects at interfaces through fabrication processes [54].

3.5. Effect of temperature

Solar cell performance parameters such as V_{oc} and J_{sc} are dependent on temperature. To analyse the effect temperature of cells is varied from 280 K to 400 K. The effect of temperature on J_{sc} and V_{oc} can be related through the following equation:

$$V_{oc} = \frac{nKT}{q} \log\left(\frac{J_{sc}}{J_o} + 1\right). \tag{3.2}$$
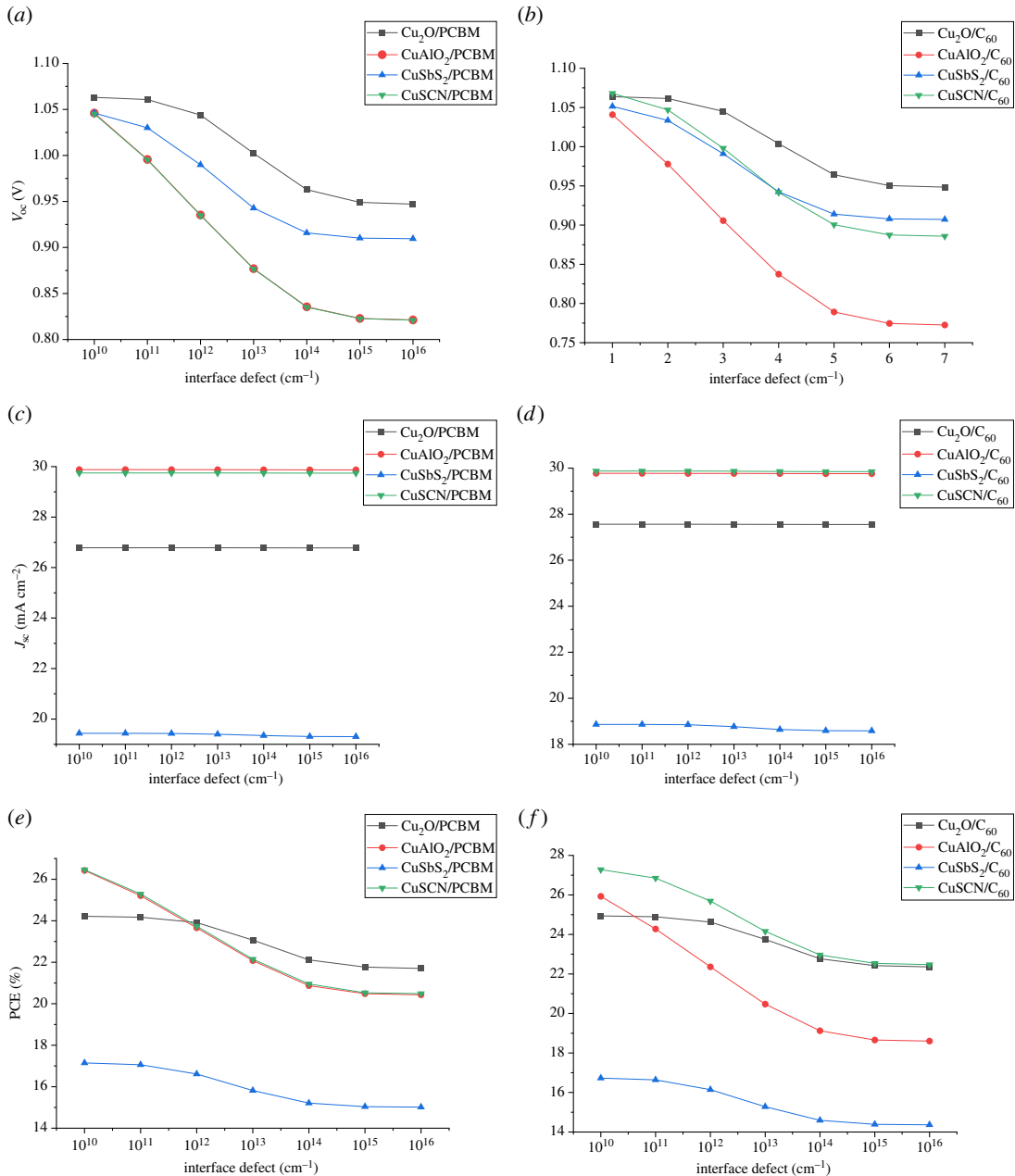
Figure 20. Effect of interface defect density at the ETL/absorber interface on (a,b) V_{oc}, (c,d) J_{sc} and (e,f) PCE.

Figure 22 shows that with the increase in temperature reverse saturation current increases exponentially which leads to the decrease in V_{oc}. As can be seen in figure 22 J_{sc} also slightly increases with temperature, which is attributed to the decrease in band gap with temperature and thus more absorption leads to an increase in J_{sc} [58,59]. The dependence of E_g on temperature in the semiconductor is described by Varshni's relation described in equation (3.3). Where $E_g(0)$ is the value of band gap at zero Kelvin temperature, α and β are material constants and T is temperature.

$$E_g(T) = E_g(0) - \frac{\alpha T^2}{(T + \beta)}.$$ (3.3)

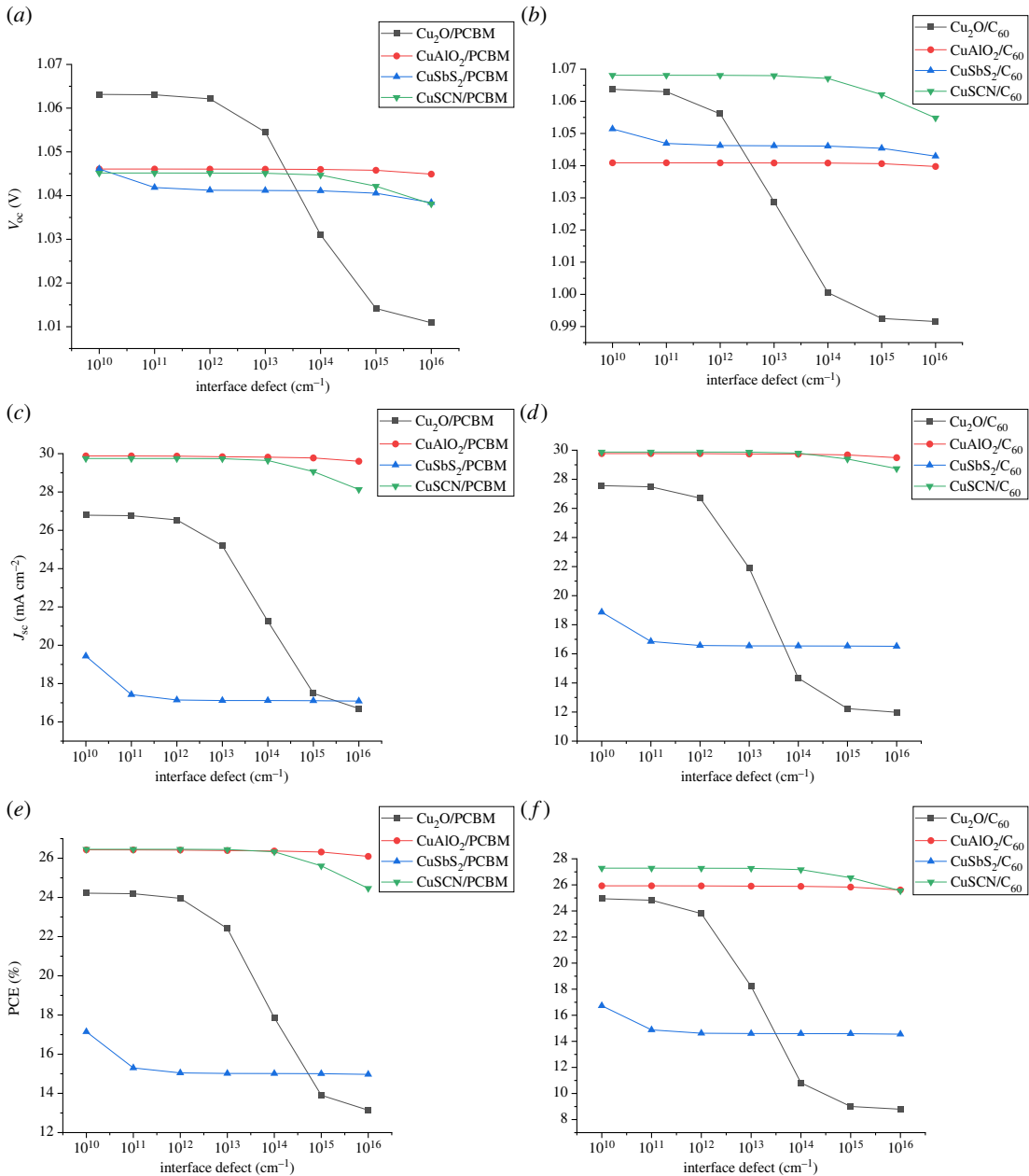PCE degradation with temperature is because of an increase in recombination mainly due to a decrease in V_{oc}.

Figure 21. Effect of interface defect density at the absorber/HTL interface on (a,b) V_{oc}, (c,d) J_{sc} and (e,f) PCE.

3.6. Effect of back contact metal electrodes

To collect the electrons by yielding built-in voltage across the solar cell, it is required for a cathode to have a proper work function. To analyse the effect of back contact on performance back, the contact work function is varied from 3.4 eV to 5 eV. Work function affects V_{oc} and PCE but it does not affect J_{sc}.

Figure 23 shows that V_{oc}, PCE and FF decrease for higher work function values, however there is no change in current. It has been observed that electrodes with low work function (3.4 eV to 4.2 eV) are suitable for FASnI$_3$-based cells because of the low band gap ($E_g = 1.41$ eV) of FASnI$_3$. Thus, it requires a low value of potential difference for charge transport and extraction across the front and back contact as compared to high band gap absorbers such as MAGeI$_3$ ($E_g 1.93$) [29,60]. The decrease in efficiency, FF and V_{oc} at higher work functions are attributed to the increase in ohmic resistance at the metal and semiconductor interface [61,62].

3.7. Effect of reflectance at back contact

Owing to the limitation of absorber thickness in solar cells, photons of larger wavelengths pass through the absorber layer without being absorbed. Reflection coatings on the back side increase the
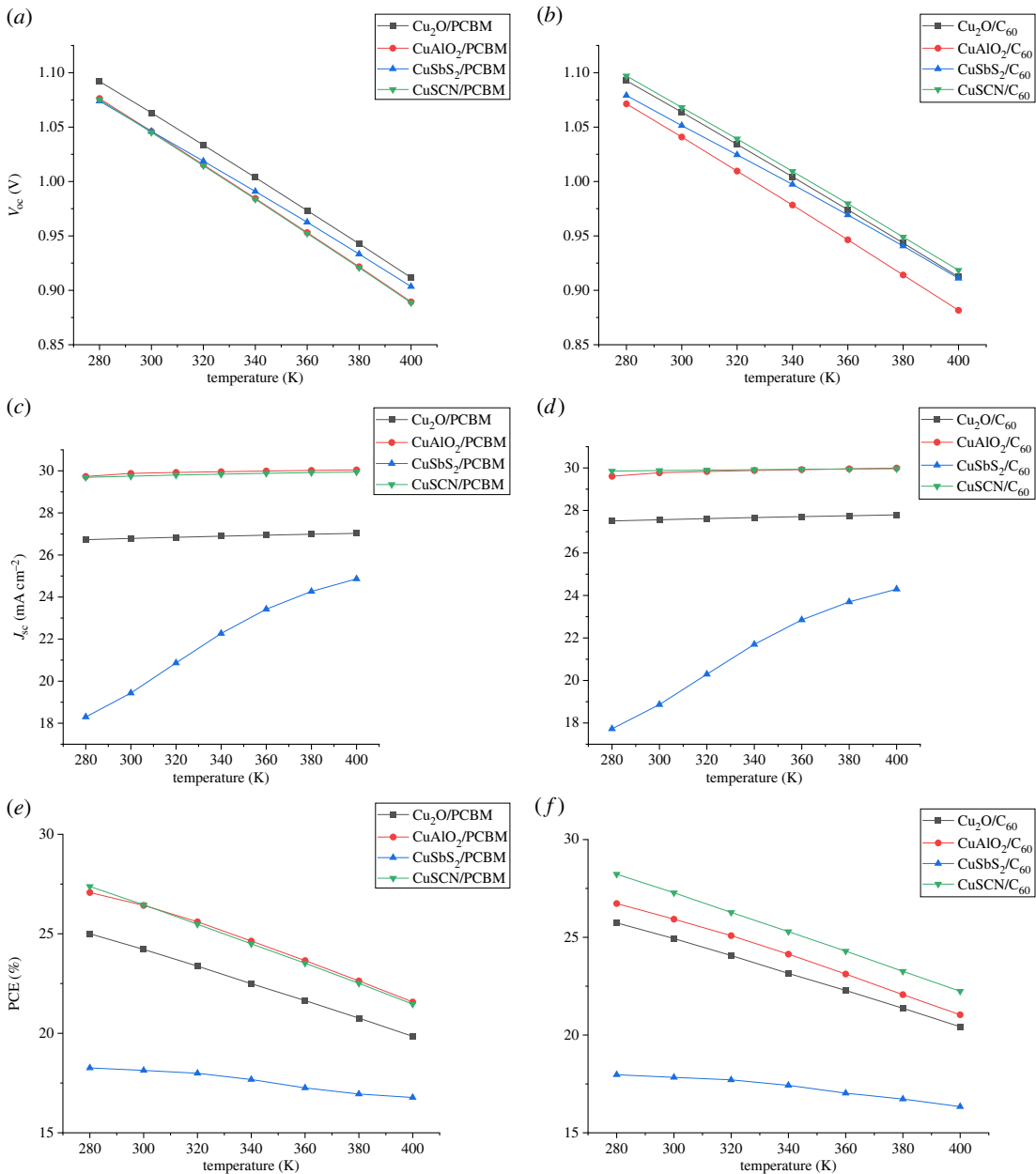
Figure 22. Effect of temperature variation on (a,b) V_{oc}, (c,d) J_{sc} and (e,f) PCE.

reflectance of the unabsorbed photons of larger wavelengths towards the absorber, thus increasing absorption probability [63]. The reflectance at back contact can be increased by using highly reflective metal with a good surface finish [64]. White paint is also used at back contact sometimes to improve reflectance [65]. To see the effect of back reflectance is varied from 10 to 95%. Figure 24 shows that the back reflection has a vital effect on the J_{sc} because no more photons absorber results in more photocurrent generation.

3.8. Comparison of performance with conventional nip architecture

To analyse the performance of ETLs and HTLs, a simulation was carried out for conventional nip architecture combinations using the optimized parameters mentioned in table 8. When comparing the results of inverted and conventional architecture it can be seen clearly that copper-based HTLs perform better in inverted combination except for CuSbS$_2$-based cells which perform better in conventional structures. The reason CuSbS$_2$ shows better results for conventional structures is because of its smaller band gap of 1.58 eV than the front ETL layers (PCBM
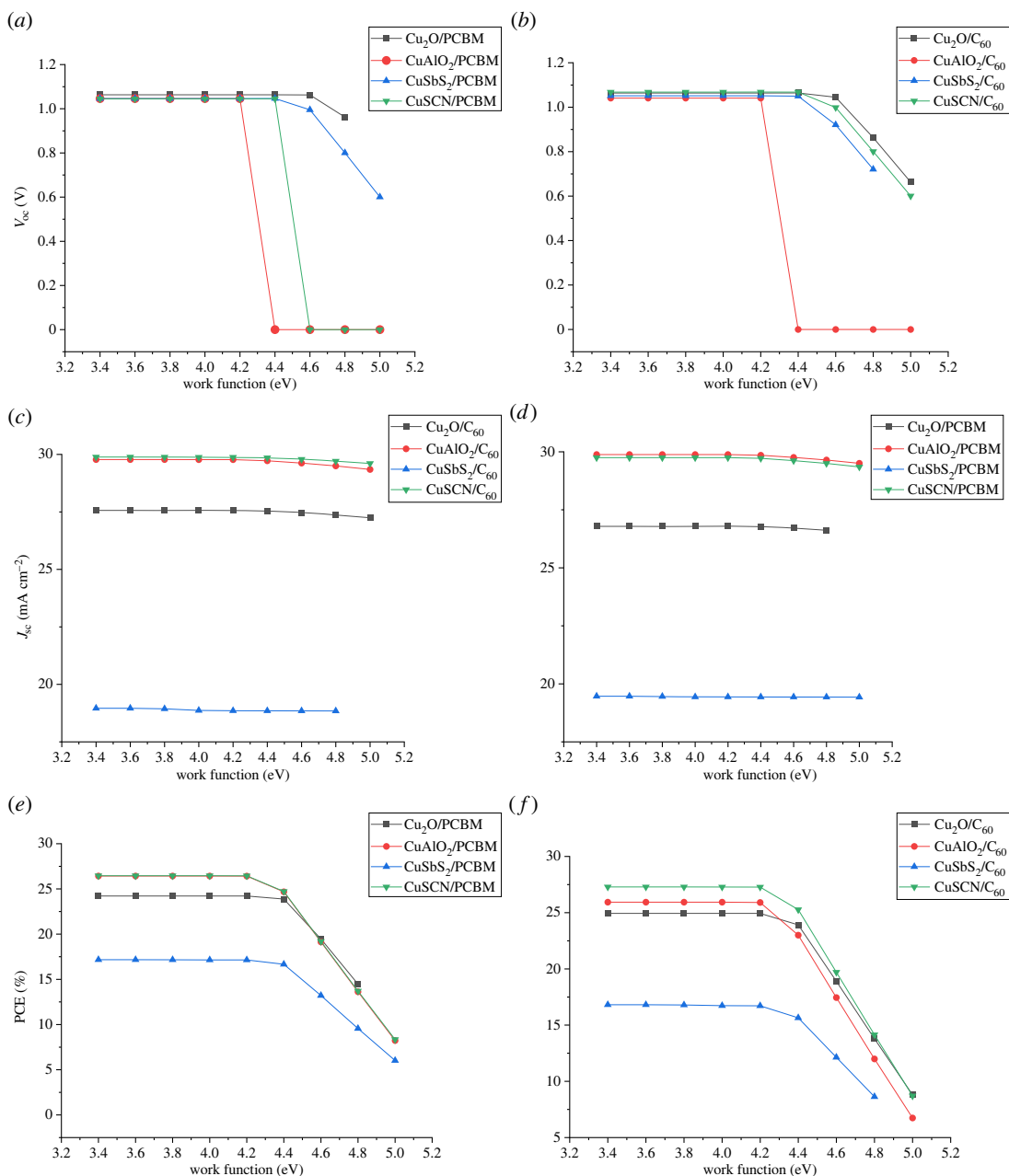
Figure 23. Effect of back contact work function on (a,b) V_{oc}, (c,d) J_{sc} and (e,f) PCE.

and C_{60}). The I–V curves for the conventional cells are shown in figure 25 and table 9 shows the performance.

3.9. Recent performance of FASnI$_3$

The recent developments in FASnI$_3$ PSC based on highest practical efficiencies reported over the years are listed in table 10. The first successful tin-based perovskite solar cell was made with an efficiency of 2.1%. It was reported using Spiro-OMeTAD as HTL and TiO$_2$ as ETL using SnF$_2$ as an additive to improve stability [11]. The following year 5.59% efficiency was obtained for ITO/PVK/PEDOT:PSS/C60/BCP/ Ag using different concentrations of SnF$_2$ [66]. Further change in structure and architecture helped to further boost the efficiency of Sn-PSC. The highest efficiency uptil 2022 is reported to be 13.82% for ITO/PEDOT:PSS/PER-grad/C$_{60}$/BCP/Ag. The sn-based PSC still has a lot of room for improvement. With the development in research and technology, this improvement can be achieved. This study shows that the Sn-PSC has the potential to surpass 20% PCE.
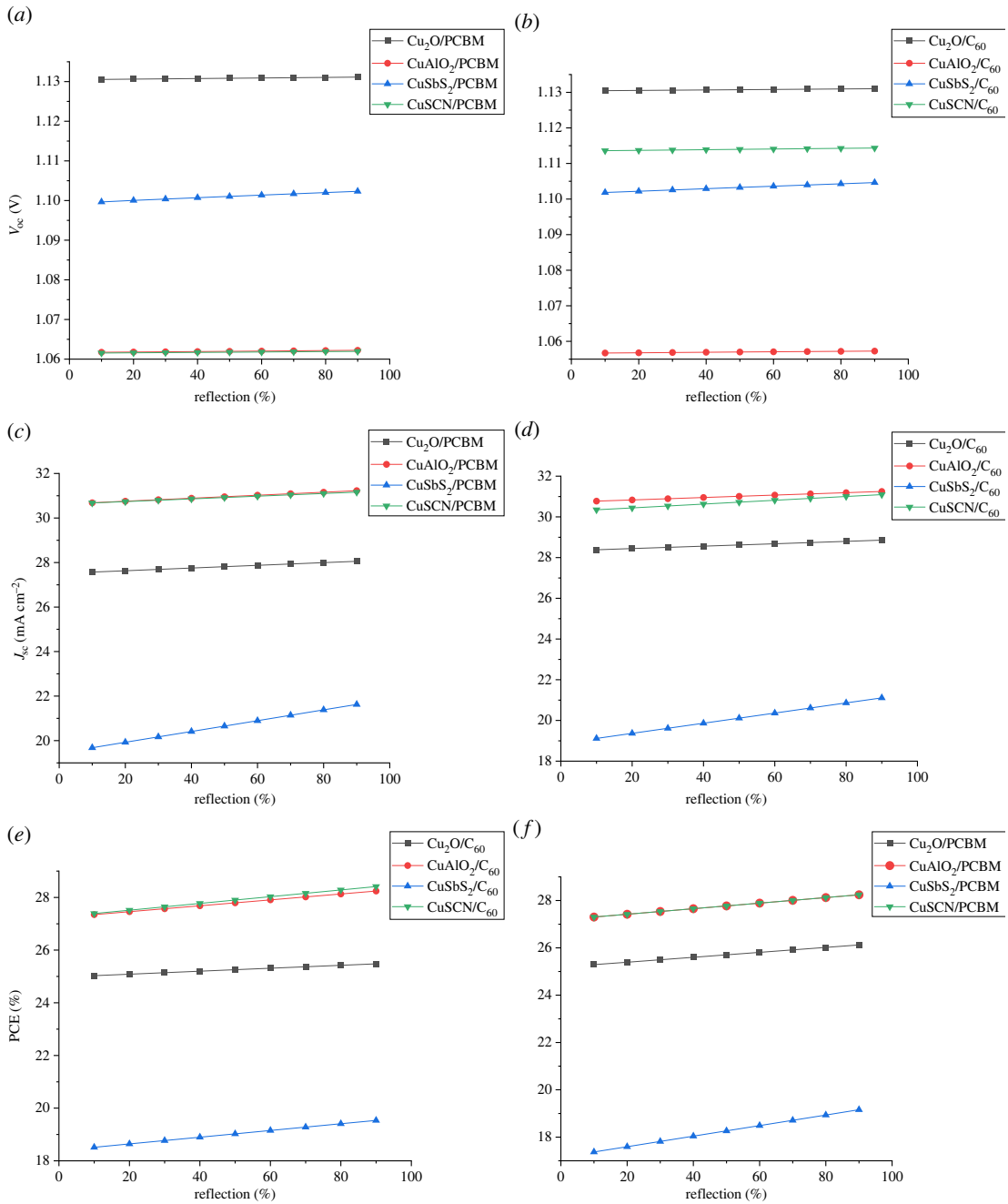
Figure 24. Effect of reflection coating on (*a,b*) V_{oc}, (*c,d*) J_{sc} and (*e,f*) PCE.

Table 9. Performance parameters of conventional nip architecture.

| cells	V_{oc}	J_{sc}	FF	PCE %
ITO/PCBM/FASnI$_3$/Cu$_2$O/Al	1.071129	27.23865	86.3444	25.192
ITO/PCBM/FASnI$_3$/CuAlO$_2$/Al	1.073057	27.03932	85.7349	24.8758
ITO/PCBM/FASnI$_3$/CuSbS$_2$/Al	1.051022	22.1453	84.4064	19.6458
ITO/PCBM/FASnI$_3$/CuSCN/Al	1.044683	23.60378	86.4641	21.3207
ITO/C$_{60}$/FASnI$_3$/Cu$_2$O/Al	1.059531	22.96424	86.181	20.969
ITO/C$_{60}$//FASnI$_3$/CuAlO$_2$/Al	1.06791	22.28187	85.6399	20.378
ITO/C$_{60}$/FASnI$_3$/CuSbS$_2$/Al	1.036739	21.87101	84.2416	19.1014
ITO/C$_{60}$/FASnI$_3$/CuSCN/Al	1.072667	24.53252	86.2043	22.6848

(a)

(b)
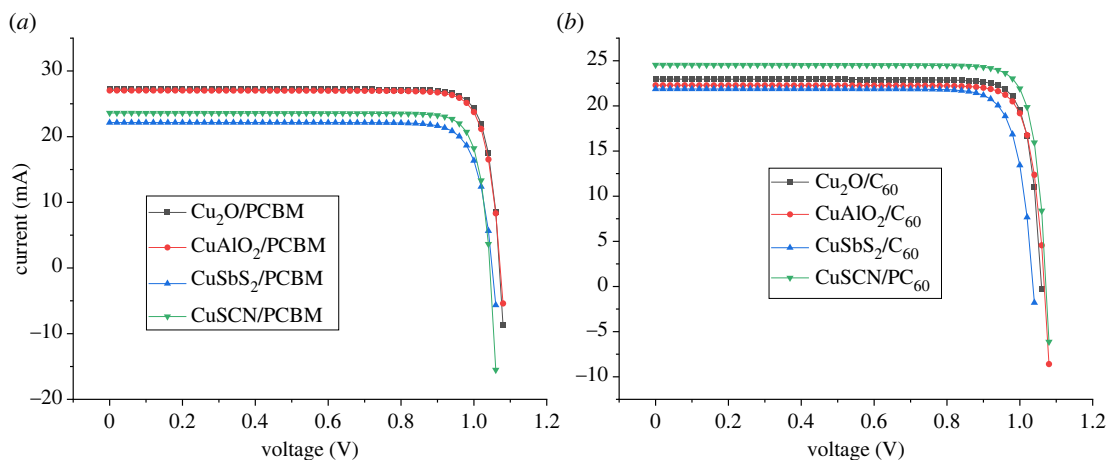
Figure 25. I–V curves of conventional nip architecture.

Table 10. Performance of best PCE achieved by FASnI$_3$ up until 2020.

device architecture	PCE (%)	year	references
TiO$_2$/PVK + 20 mol%SnF$_2$/spiro-OMeTAD/Au	2.1	2015	[11]
ITO/PEDOT:PSS/ PVK + 10 mol%; SnF$_2$/C60/BCP/Ag	5.59	2016	[66]
FTO/c − TiO$_2$/m− TiO$_2$/[PVK + 10 mol%; en/PTAA/Au	7.14	2017	[67]
ITO/PEDOT:PSS/PVK(π-conjugated)/C$_{60}$/BCP/Ag	10.1	2019	[68]
ITO/PEDOT:PSS/PVK+50% LFA/C$_{60}$/BCP/Ag	10.37	2020	[69]
ITO/PEDOT:PSS/PVK-PNCs/C$_{60}$/BCP/Ag	11.39%	2021	[70]
ITO/PEDOT:PSS/PVK-grad/C$_{60}$/Ag	13.82%	2022	[20]

4. Conclusion

In this study, eight inverted p-i-n novel FASnI$_3$-based solar cells were numerically modelled, optimized and studied in detail. The effect of thickness, doping, defect density, temperature, interface defects, work function and the reflective coating on the performance parameters of solar cells is explained in detail. Recombination electric potential band alignment is explained in detail for absorber/HTL and ETL/absorber interfaces. QE and absorption curves are related to the band gap of HTL. It has been concluded that the performance of solar cells increases with the absorber thickness up to a certain point (optimized value) after which saturation is achieved and then it declines. Most of the cells were optimized for different thickness values ranging from 350 to 1000 nm. Moreover, it has been observed that ETL thickness has a negligible effect on the performance of the solar cell. ETL thickness is kept at 100 nm for all cells. Absorber doping for all cells optimization is achieved at 10^{16} as for most cells the performance decreases at high doping due to an increase in impurity scattering. As for CTLs, doping performance of all the cells increased because of an increase in majority charge carriers. Absorber defects and interface decrease cell performance drastically. From optimization, the best performance for Group 1 was achieved by ITO/CuSCN/FASnI$_3$/C$_{60}$/Al with PCE of 27.26% and for Group 2 the best efficiency was achieved by (ITO/CuAlO$_2$/FASnI$_3$/PCBM/Al) with efficiency of 27.16% due to highly conductive copper-based HTLs and perfect band alignment with FASnI$_3$ and high electric potential values at interfaces. It is concluded that in p-i-n inverted cells, the HTLs with larger band gaps are preferred to achieve transparency at the front. All copper-based materials proved to be promising candidates and showed higher electric potential and less recombination at absorber/HTL interfaces except for CuSbS$_2$. CuSbS$_2$, having a smaller E_g of 1.58 than both ETLs (C$_{60}$ and PCBM), behaves better in the conventional structure. Furthermore, the effect

of back contact work function is studied and it is concluded that the metals with work functions lower than 4.2 are suitable for these cells for the reason that aluminum was considered a suitable choice. As temperature increases, the solar cell performance deteriorates, and for reflection coating the performance of the solar cell increases.

Authors' contributions. M.Ismail: data curation, formal analysis, investigation, writing—original draft; M.N.: conceptualization, formal analysis, methodology, project administration, supervision, writing—review and editing; S.T.J.: conceptualization, data curation, formal analysis, investigation, methodology, writing—original draft, writing—review and editing; M.Imran: investigation, supervision, validation, visualization, writing—review and editing.

All authors gave final approval for publication and agreed to be held accountable for the work performed therein.

References

1. Zhang X et al. 2021 Rapid degradation behavior of encapsulated perovskite solar cells under light, bias voltage or heat fields. Nanoscale Adv. 3, 6128–6137. (doi:10.1039/d1na00495f)

2. Hamed MSG, Mola GT. 2019 Mixed halide perovskite solar cells : progress and challenges. Crit. Rev. Solid State Mater. Sci. 45, 85–112. (doi:10.1080/10408436.2018.1549976)

3. Park NG, Grätzel M, Miyasaka T. 2016 Organic-Inorganic Halide Perovskite Photovoltaics, pp. 1–366. Cham, Switzerland: Springer.

4. Zhou D, Zhou T, Tian Y, Zhu X, Tu Y. 2018 Perovskite-Based Solar Cells: Materials, Methods, and Future Perspectives. J. Nanomater. 2018, 1–15. (doi:10.1155/2018/8148072)

5. The National Renewable Energy Laboratory NREL. 2022 Best Research-Cell Efficiency Chart | Photovoltaic Research | https://www.nrel.gov/pv/cell-efficiency.html.

6. Ren M, Qian X, Chen Y, Wang T, Zhao Y. 2022 Potential lead toxicity and leakage issues on lead halide perovskite photovoltaics. J. Hazard. Mater. 426, 127848. (doi:10.1016/J.JHAZMAT.2021.127848)

7. Kour R, Arya S, Verma S, Gupta J, Bandhoria P. 2019 Potential substitutes for replacement of lead in perovskite solar cells : a review. Global Challenges 3, 1900050. (doi:10.1002/gch2.201900050)

8. Wang F, Ma J, Xie F, Li L, Chen J, Fan J, Zhao N. 2016 Organic cation-dependent degradation mechanism of organotin halide perovskites. Adv. Funct. Mater. 26, 3417–3423. (doi:10.1002/adfm.201505127)

9. Dixit H, Punetha D, Pandey SK. 2019 Improvement in performance of lead free inverted perovskite solar cell by optimization of solar parameters. Optik (Stuttg). 179, 969–976. (doi:10.1016/j.ijleo.2018.11.028)

10. Roy P, Tiwari S, Khare A. 2021 An investigation on the influence of temperature variation on the performance of tin (Sn) based perovskite solar cells using various transport layers and absorber layers. Results Opt. 4, 100083. (doi:10.1016/j.rio.2021.100083)

11. Koh TM, Krishnamoorthy T, Yantara N, Shi C, Leong WL, Boix PP, Grimsdale AC, Mhaisalkar SG, Mathews N. 2015 Formamidinium tin-based perovskite with low Eg for photovoltaic applications. J. Mater. Chem. A 3, 14 996–15 000. (doi:10.1039/c5ta00190k)

12. Tara A, Bharti V, Sharma S, Gupta R. 2021 Device simulation of FASnI3 based perovskite solar cell with Zn(00.3, S0.7) as electron transport layer using SCAPS-1D. Opt. Mater. (Amst). 119, 111362. (doi:10.1016/j.optmat.2021.111362)

13. Tonui P, Oseni SO, Sharma G, Yan Q, Tessema Mola G. 2018 Perovskites photovoltaic solar cells: an overview of current status. Renew. Sustain. Energy Rev. 91, 1025–1044. (doi:10.1016/j.rser.2018.04.069)

14. Zhang Y et al. 2023 Highly efficient and stable FA-based quasi-2D Ruddlesden–Popper perovskite solar cells by the incorporation of β-fluorophenylethanamine cations. Adv. Mater. 35, 2210836. (doi:10.1002/ADMA.202210836)

15. Shah SAA, Sayyad MH, Khan K, Guo K, Shen F, Sun J, Tareen AK, Gong Y, Guo Z. 2020 Progress towards high-efficiency and stable tin-based perovskite solar cells. Energies 13, 5092. (doi:10.3390/en13195092)

16. Abdelaziz S, Zekry A, Shaker A, Abouelatta M. 2020 Investigating the performance of formamidinium tin-based perovskite solar cell by SCAPS device simulation. Opt. Mater. (Amst). 101, 109738. (doi:10.1016/j.optmat.2020.109738)

17. Saidaminov MI et al. 2018 Suppression of atomic vacancies via incorporation of isovalent small ions to increase the stability of halide perovskite solar cells in ambient air. Nat. Energy 3, 648–654. (doi:10.1038/S41560-018-0192-2)

18. Azhakanantham D, Selvamani M, Geun Kim T, Contreras D, Varman Kesavan A. 2022 Exploring novel HTL suitable for eco-friendly and high performance FASnI3 photovoltaics. Mater. Sci. Eng. B Solid-State Mater. Adv. Technol. 284, 115909. (doi:10.1016/j.mseb.2022.115909)

19. Jiang X et al. 2021 Supplementary Materials for One-step Synthesis of SnI 2 ·(DMSO) x Adducts for High-Performance Tin Perovskite Solar Cells.

20. Wu T, Liu X, Luo X, Segawa H, Tong G, Zhang Y, Ono LK, Qi Y, Han L. 2022 Heterogeneous FASnI3 absorber with enhanced electric field for high-performance lead-free perovskite solar cells. Nano-Micro Lett. 14, 99. (doi:10.1007/s40820-022-00842-4)

21. Gangala S, Misra R. 2018 Spiro-linked organic small molecules as hole-transport materials for perovskite solar cells. J. Mater. Chem. A 6, 18 750–18 765. (doi:10.1039/c8ta08503j)

22. Xia Y, Dai S. 2021 Review on applications of PEDOTs and PEDOT:PSS in perovskite solar cells. J. Mater. Sci. Mater. Electron. 32, 12 746–12 757. (doi:10.1007/s10854-020-03473-w)

23. Bidikoudi M, Kymakis E. 2019 Novel approaches and scalability prospects of copper based hole transporting materials for planar perovskite solar cells. J. Mater. Chem. C 7, 13 680–13 708. (doi:10.1039/c9tc04009a)

24. Al Mamun A, Ava TT, Zhang K, Baumgart H, Namkoong G. 2017 New PCBM/carbon based electron transport layer for perovskite solar cells. Phys. Chem. Chem. Phys. 19, 17 960–17 966. (doi:10.1039/c7cp02523h)

25. Xu J, Shi X, Chen J, Luan J, Yao J. 2019 Optimizing solution-processed C60 electron transport layer in planar perovskite solar cells by interfacial modification with solid-state ionic-liquids. J. Solid State Chem. 276, 302–308. (doi:10.1016/J.JSSC.2019.05.027)

26. Yang B, Peng S, Choy WCH. 2021 Inorganic top electron transport layer for high performance inverted perovskite solar cells. EcoMat 3, 1–24. (doi:10.1002/eom2.12127)

27. Ma S, Gu X, Kyaw AK, Wang DH, Priya S, Ye T. 2021 Fully inorganic CsSnI3-based solar cells with >6% efficiency and enhanced stability enabled by mixed electron transport layer. ACS Appl. Mater. Interfaces 13, 1345–1352. (doi:10.1021/acsami.0c16634)

28. Zhang C, Qi L, Chen Q, Lv L, Ning Y, Hu Y, Hou Y, Teng F. 2014 Plasma treatment of ITO cathode to fabricate free electron selective layer

in inverted polymer solar cells. *J. Mater. Chem. C* **2**, 8715–8722. (doi:10.1039/c4tc01777c)

29. D. Jayan K, Sebastian V. 2021 Comparative study on the performance of different lead-based and lead-free perovskite solar cells. *Adv. Theory Simul.* **4**, 1–11. (doi:10.1002/adts.202100027)

30. Singh N, Agarwal A, Agarwal M. 2021 Performance evaluation of lead–free double-perovskite solar cell. *Opt. Mater. (Amst).* **114**, 1–11. (doi:10.1016/j.optmat.2021.110964)

31. Li S *et al.* 2019 The investigation of inverted p-i-n planar perovskite solar cells based on FASnI3 films. *Sol. Energy Mater. Sol. Cells* **199**, 75–82. (doi:10.1016/j.solmat.2019.04.023)

32. Kumar D, Kuchhal P. 2021 Optimization of photovoltaic conversion performance of a TiO_2 based dye sensitized solar cells (DSSCs) Optimization of photovoltaic conversion performance of a TiO_2 based dye sensitized solar cells (DSSCs). *Eng. Res. Express* **3**, 045021.

33. Nykyruy LI, Yavorskyi RS, Zapukhlyak ZR, Wisz G, Potera P. 2019 Evaluation of CdS/CdTe thin film solar cells: SCAPS thickness simulation and analysis of optical properties. *Opt. Mater. (Amst).* **92**, 319–329. (doi:10.1016/j.optmat.2019.04.029)

34. Mahmood W, Ali J, Zahid I, Thomas A, ul Haq A. 2018 Optical and electrical studies of CdS thin films with thickness variation. *Optik (Stuttg).* **158**, 1558–1566. (doi:10.1016/j.ijleo.2018.01.045)

35. Mahmood W, Ali J, Thomas A, Awan S, Jackman M, Haq A-, Hassan MU, Shah NA. 2018 Role of Ag1+ substitutional defects on the electronic and optical properties of n-type CdS thin films semiconductor for sustainable and stable window layer in solar cells technology. *Opt. Mater. (Amst).* **85**, 143–152. (doi:10.1016/j.optmat.2018.08.056)

36. Santiago Tepantlán C, Pérez González AM, Valeriano Arreola I. 2008 Structural, optical and electrical properties of CdS thin films obtained by spray pyrolysis. *Rev. Mex. Fis.* **54**, 112–117.

37. Li S, Cao YL, Li WH, Bo ZS. 2021 A brief review of hole transporting materials commonly used in perovskite solar cells. *Rare Met.* **40**, 2712–2729. (doi:10.1007/s12598-020-01691-z)

38. Khattak YH, Baig F, Toura H, Beg S, Soucase BM. 2019 CZTSe kesterite as an alternative hole transport layer for MASnI₃ perovskite solar cells. *J. Electron. Mater.* **48**, 5723–5733. (doi:10.1007/s11664-019-07374-5)

39. Ahmed A, Riaz K, Mehmood H, Tauqeer T, Ahmad Z. 2020 Performance optimization of CH3NH3Pb(I1-xBrx)3 based perovskite solar cells by comparing different ETL materials through conduction band offset engineering. *Opt. Mater. (Amst).* **105**, 109897. (doi:10.1016/j.optmat.2020.109897)

40. Ding C *et al.* 2018 Effect of the conduction band offset on interfacial recombination behavior of the planar perovskite solar cells. *Nano Energy* **53**, 17–26. (doi:10.1016/j.nanoen.2018.08.031)

41. Gansukh M *et al.* 2020 Energy band alignment at the heterointerface between CdS and Ag-alloyed CZTS. *Sci. Rep.* **10**, 1–11. (doi:10.1038/s41598-020-73828-0)

42. Zhao P, Lin Z, Wang J, Yue M, Su J, Zhang J, Chang J, Hao Y. 2019 Numerical simulation of planar heterojunction perovskite solar cells

based on SnO2 electron transport layer. *ACS Appl. Energy Mater.* **2**, 4504–4512. (doi:10.1021/acsaem.9b00755)

43. Kearney K, Seo G, Matsushima T, Adachi C, Ertekin E, Rockett A. 2018 Computational analysis of the interplay between deep level traps and perovskite solar cell efficiency. *J. Am. Chem. Soc.* **140**, 15 655–15 660. (doi:10.1021/jacs.8b06002)

44. Haddad J, Krogmeier B, Klingebiel B, Krückemeier L, Melhem S, Liu Z, Hüpkes J, Mathur S, Kirchartz T. 2020 Analyzing interface recombination in lead-halide perovskite solar cells with organic and inorganic hole-transport layers. *Adv. Mater. Interfaces* **7**, 2000366. (doi:10.1002/admi.202000366)

45. Pazos-Outón LM, Xiao TP, Yablonovitch E. 2018 Fundamental efficiency limit of lead iodide perovskite solar cells. *J. Phys. Chem. Lett.* **9**, 1703–1711. (doi:10.1021/acs.jpclett.7b03054)

46. Bag A, Radhakrishnan R, Nekovei R, Jeyakumar R. 2020 Effect of absorber layer, hole transport layer thicknesses, and its doping density on the performance of perovskite solar cells by device simulation. *Sol. Energy* **196**, 177–182. (doi:10.1016/j.solener.2019.12.014)

47. Tariq Jan S, Noman M. 2022 Influence of layer thickness, defect density, doping concentration, interface defects, work function, working temperature and reflecting coating on lead-free perovskite solar cell. *Sol. Energy* **237**, 29–43. (doi:10.1016/j.solener.2022.03.069)

48. Abdi-Jalebi M, Ibrahim Dar M, Sadhanala A, Senanayak SP, Grätzel M, Friend RH. 2017 Monovalent cation doping of $CH_3NH_3PbI_3$ for efficient perovskite solar cells. *J. Vis. Exp.* **2017**, 1–9. (doi:10.3791/55307)

49. Gamal N, Sedky SH, Shaker A, Fedawy M. 2021 Design of lead-free perovskite solar cell using Zn1-xMgxO as ETL: SCAPS device simulation. *Optik (Stuttg).* **242**, 167306. (doi:10.1016/j.ijleo.2021.167306)

50. Ščajev P, Mekys A, Subačius L, Stanionytė S, Kuciauskas D, Lynn KG, Swain SK. 2022 Impact of dopant-induced band tailing on optical spectra, charge carrier transport, and dynamics in single-crystal CdTe. *Sci. Rep.* **12**, 1–10. (doi:10.1038/s41598-022-16994-7)

51. Adeleye D, Lomuscio A, Sood M, Siebentritt S. 2021 Lifetime, quasi-Fermi level splitting and doping concentration of Cu-rich CuInS₂ absorbers. *Mater. Res. Express* **8**, 025905. (doi:10.1088/2053-1591/abe3c1)

52. Chen D, Wang Y, Lin Z, Huang J, Chen XZ, Pan D, Huang F. 2010 Growth strategy and physical properties of the high mobility p-type cui crystal. *Cryst. Growth Des.* **10**, 2057–2060. (doi:10.1021/cg100270d)

53. Chen Y, Shen H, Altermatt PP. 2014 Analysis of recombination losses in screen-printed aluminum-alloyed back surface fields of silicon solar cells by numerical device simulation. *Sol. Energy Mater. Sol. Cells* **120**, 356–362. (doi:10.1016/j.solmat.2013.05.051)

54. Sherkar TS, Momblona C, Gil-escrig L, Sessolo M, Bolink HJ, Koster LJA. 2017 Recombination in perovskite solar cells : significance of grain boundaries, interface traps and defect ions. *ACS Energy Letters* **2**, 1214–1222.

55. Mahjabin S *et al.* 2020 Perceiving of defect tolerance in perovskite absorber layer for efficient perovskite solar cell. *IEEE Access* **8**, 106 346–106 353. (doi:10.1109/ACCESS.2020.3000217)

56. Chen J, Park NG. 2019 Causes and solutions of recombination in perovskite solar cells. *Adv. Mater.* **31**, 1–56. (doi:10.1002/adma.201803019)

57. Basyoni MSS, Salah MM, Mousa M, Shaker A, Zekry A, Abouelatta M, Alshammari MT, Al-Dhlan KA, Gontrand C. 2021 On the investigation of interface defects of solar cells: lead-based vs lead-free perovskite. *IEEE Access* **9**, 130 221–130 232. (doi:10.1109/ACCESS.2021.3114383)

58. Lin L, Ravindra NM. 2020 Temperature dependence of CIGS and perovskite solar cell performance: an overview. *SN Appl. Sci.* **2**, 1–12. (doi:10.1007/s42452-020-3169-2)

59. Chakraborty K, Choudhury MG, Paul S. 2019 Numerical study of Cs2TiX6 (X = Br−, I−, F− and Cl−) based perovskite solar cell using SCAPS-1D device simulation. *Sol. Energy* **194**, 886–892. (doi:10.1016/j.solener.2019.11.005)

60. Li CS, Cheng T-C, Shen S-W, Wu Y-T, Cheng J-R, Ni I-C, Chen M-H, Wu C-I. 2019 Influence of work function of carrier transport materials with perovskite on switchable photovoltaic phenomena. *J. Phys. Chem. C.* **123**, 28668–28676. (doi:10.1021/acs.jpcc.9b06106)

61. Behrouznejad F, Shahbazi S, Taghavinia N, Wu HP, Wei-Guang Diau E. 2016 A study on utilizing different metals as the back contact of $CH_3NH_3PbI_3$ perovskite solar cells. *J. Mater. Chem. A* **4**, 13 488–13 498. (doi:10.1039/c6ta05938d)

62. Lim KG, Ahn S, Kim H, Choi MR, Huh DH, Lee TW. 2016 Self-doped conducting polymer as a hole-extraction layer in organic-inorganic hybrid perovskite solar cells. *Adv. Mater. Interfaces* **3**, 1–7. (doi:10.1002/admi.201500678)

63. Santbergen R, van Zolingen RJC. 2008 The absorption factor of crystalline silicon PV cells: a numerical and experimental study. *Sol. Energy Mater. Sol. Cells* **92**, 432–444. (doi:10.1016/j.solmat.2007.10.005)

64. Iles PA, Chu CL. 1996 Use of high back surface reflectance in PV cell design. In *Conf. Rec. IEEE Photovolt. Spec. Conf., Washington, DC, 13–17 May 1996, pp. 109–112.* New York, NY: IEEE. (doi:10.1109/PVSC.1996.563959)

65. Berger O, Inns D, Aberle AG. 2007 Commercial white paint as back surface reflector for thin-film solar cells. *Sol. Energy Mater. Sol. Cells* **91**, 1215–1221. (doi:10.1016/j.solmat.2007.04.008)

66. Liao W *et al.* 2016 Lead-free inverted planar formamidinium tin triiodide perovskite solar cells achieving power conversion efficiencies up to 6.22%. *Adv. Mater.* **28**, 9333–9340. (doi:10.1002/ADMA.201602992)

67. Ke W, Stoumpos CC, Spanopoulos I, Mao L, Chen M, Wasielewski MR, Kanatzidis MG. 2017 Efficient lead-free solar cells based on hollow {en}MASnI₃ perovskites. *J. Am. Chem. Soc.* **139**, 14 800–14 806. (doi:10.1021/jacs.7b09018)

68. Wu T, Liu X, He X, Wang Y, Meng X, Noda T, Yang X, Han L. 2020 Efficient and stable tin-based perovskite solar cells by introducing π-conjugated Lewis base. *Sci. China Chem.* **63**, 107–115. (doi:10.1007/s11426-019-9653-8)

69. Scaife DE, Weller PF, Fisher WG. 1974 Crystal preparation and properties of cesium tin(II) trihalides. *J. Solid State Chem.* **9**, 308–314. (doi:10.1016/0022-4596(74)90088-7)

70. Meng X *et al.* 2021 Crystallization kinetics modulation of FASnI$_3$ films with pre-nucleation clusters for efficient lead-free perovskite solar cells. *Angew. Chemie - Int. Ed.* **60**, 3693–3698. (doi:10.1002/anie.202012280)

71. Ismail M, Noman M, Tariq Jan S, Imran M. 2023 Data from: Boosting efficiency of eco-friendly perovskite solar cell through optimization of novel charge transport layers. Dryad Digital Repository. (doi:10.5061/dryad.4j0zpc8h9)